remote sensing

MDPI

Article

Integrated Landslide Risk Assessment via a Landslide Susceptibility Model Based on Intelligent Optimization Algorithms

Xin Dai [1,2], Jianping Chen [1,2,*], Tianren Zhang [3] and Chenli Xue [1,2]

[1] School of Earth Sciences and Resources, China University of Geosciences, Beijing 100083, China; daixin@email.cugb.edu.cn (X.D.)
[2] Beijing Key Laboratory of Development and Research for Land Resources Information, Beijing 100083, China
[3] School of Energy Science and Engineering, University of Science and Technology of China, Hefei 230026, China
* Correspondence: 3s@cugb.edu.cn

Abstract: Accurate and objective regional landslide risk assessment is crucial for the precise prevention of regional disasters. This study proposes an integrated landslide risk assessment via a landslide susceptibility model based on intelligent optimization algorithms. By simulating the process of rime frost formation, it effectively selects features and assigns weights, overcoming the overfitting issue faced by XGBoost in handling high-dimensional features. By integrating the concepts of landslide susceptibility, dynamic landslide factors, and social vulnerability, an integrated landslide risk index was developed. Further investigation was conducted on how landslide susceptibility results influence risk, identifying regions with varying levels of landslide risk due to spatial heterogeneity in geological background, natural environment, and socio-economic conditions. This study's results demonstrate that the RIME-XGBoost landslide susceptibility model exhibits superior stability and accuracy, achieving an AUC score of 0.947, which represents an improvement of 0.064 compared to the unoptimized XGBoost model, while the accuracy shows a maximum increase of 0.15 relative to other models. Additionally, an analysis using cloud theory indicates that the model's expectation and hyper-entropy are minimized. High-risk-level areas, constituting only 1.26% of the total area, are predominantly located in densely populated, economically developed urban regions, where roads and rivers are the key influencing factors. In contrast, low-risk areas, which cover approximately 72% of the total area, are more broadly distributed. The landslide susceptibility predictions notably influence high-risk regions with concentrated populations.

Keywords: landslide risk; landslide susceptibility; XGBoost; rime optimization algorithm; remote sensing

check for updates

Academic Editor: Gianluca Groppelli

Received: 22 October 2024
Revised: 27 December 2024
Accepted: 3 February 2025
Published: 5 February 2025

Citation: Dai, X.; Chen, J.; Zhang, T.; Xue, C. Integrated Landslide Risk Assessment via a Landslide Susceptibility Model Based on Intelligent Optimization Algorithms. *Remote Sens.* **2025**, *17*, 545. https://doi.org/10.3390/rs17030545

Copyright: © 2025 by the authors. Licensee MDPI, Basel, Switzerland. This article is an open access article distributed under the terms and conditions of the Creative Commons Attribution (CC BY) license (https://creativecommons.org/licenses/by/4.0/).

1. Introduction

Landslides are among the most serious and common geological hazards in the world [1–4]. They are widely distributed and characterized by high frequency, suddenness, rapid movement, and devastation [5,6], directly threatening human safety, livelihood stability, agricultural output, livestock survival, and the ecological balance of forests globally [7–9]. According to the Global Natural Disasters Report 2020, landslides have become the deadliest natural disaster in Myanmar [10]. The United Nations Office for the Coordination of Humanitarian Affairs (UNOCHA) stated that from 6 to 13 August 2019,

numerous countries in the Asia–Pacific region were hit by consecutive landslides, resulting in many casualties and missing persons and causing considerable damage to houses, crops, etc., and heavy economic losses [11]. Statistics show that from 2004 to 2016, a total of 4862 landslides occurred worldwide, resulting in 55,997 deaths [12]. In China, landslides have killed over 25,000 people in the past 60 years, causing economic losses of up to USD 50 million annually [13]. Moreover, the number of new landslide disasters continues to increase rapidly [14,15]. Given the enormous impact of landslide hazards, they have become the focus of research in the field of geohazards globally, and the identification and assessment of landslide risk have become an important foundation for landslide prevention and emergency management responses [16].

Landslide susceptibility assessment is a key aspect of geohazard risk prevention and mitigation. By employing accurate and reliable evaluation techniques, it effectively identifies high-susceptibility areas, providing a scientific basis for disaster prevention and reduction. Currently, landslide susceptibility assessment methods are primarily divided into knowledge-driven and data-driven approaches [17]. Knowledge-driven methods [18] are based on expert experience, combining subjective judgment and qualitative analysis for assessment. However, these methods often suffer from subjectivity and a lack of reproducibility, with techniques like the analytic hierarchy process (AHP) [19] and fuzzy comprehensive evaluation (FCE) [20] being typical examples. In contrast, data-driven methods [21] leverage modern statistical analysis and machine learning techniques to uncover latent patterns and associative features of landslide occurrences from large-scale data, resulting in more objective and accurate evaluations. In recent years, with the rapid development of artificial intelligence, data-driven methods have gained widespread application in landslide susceptibility assessment, resulting in various statistical models and machine learning evaluation methods. Commonly used statistical analysis methods include information value (IV) [22], frequency ratio (FR) [23], and weight of evidence (WOE) [24]. However, due to the complexity of landslide formation mechanisms, the accuracy of these traditional statistical methods is subject to certain limitations [25]. To enhance predictive performance, researchers have introduced machine learning models, such as random forest (RF) [26], support vector machines (SVMs) [27], and convolutional neural networks (CNNs) [28]. These models, with their exceptional adaptive learning capabilities, can effectively capture the complex nonlinear relationships between landslide events and influencing factors [29]. Jiang et al. [30] compared the performance of various machine learning methods, including CNNs, naive Bayes, and decision trees (DTs), in predicting landslide susceptibility in the Hongxi River Basin, Pingwu County, China. Huang et al. [31] introduced the Conv-SE-LSTM model for landslide susceptibility prediction, demonstrating its superior performance over SVMs, CNNs, and long short-term memory (LSTM). The machine learning models in the aforementioned studies are capable of learning hidden patterns within the data, thereby improving the accuracy and reliability of landslide susceptibility assessment. However, most research focuses on comparing different machine learning models to evaluate their performance advantages and limitations.

Extreme gradient boosting (XGBoost), a typical ensemble algorithm, combines multiple decision trees and features parallelization, distributed computing, cache optimization, and out-of-core processing, which enhance its computational speed, accuracy, and stability. Janizadeh et al. [32] used XGBoost and RF models to map the spatiotemporal changes in landslide susceptibility under four future scenarios in Iran. Shua et al. [33] trained and tested the initial dataset using the XGBoost model to generate a landslide susceptibility map, classifying it into very low, low, moderate, high, and very high susceptibility levels. Zhang et al. [34] studied the performance of the XGBoost classifier in evaluating landslide

susceptibility and compared its applicability in Fengjie County, a typical landslide-prone area in Southwestern China.

The above studies explored the impact of XGBoost on landslide susceptibility prediction. However, model accuracy is influenced not only by the chosen machine learning algorithm but also by pre-set parameter values. Studies have shown that combining multiple models can yield better results [35–37]. To improve model accuracy, parameters should be fine-tuned based on regional characteristics and data features, thereby optimizing the model structure and enhancing evaluation precision. Sun et al. [38] optimized RF and LR using Bayesian algorithms to produce more accurate landslide susceptibility maps. Le et al. [39] optimized the XGBoost model using particle swarm optimization (PSO) to assess the thermal load of urban buildings. Ding et al. [40] optimized the XGBoost model parameters using the Bayesian algorithm to identify small faults in seismic interpretation. Currently, research on optimizing the XGBoost model for landslide susceptibility has not received sufficient attention. To further improve the accuracy of landslide susceptibility assessment, this study proposes optimizing XGBoost using the rime optimization algorithm (RIME) to construct the RIME-XGBoost landslide susceptibility model. RIME is an optimization algorithm newly proposed by Su et al. in 2023 [41]. Inspired by the rime ice growth mechanism, the algorithm simulates the movement of soft frost ice particles to establish an optimized search strategy. Compared to the traditional sparrow search algorithm (SSA) and PSO algorithm, which are prone to local optima, the RIME introduces new solutions to improve search space coverage, maintaining algorithm diversity and enhancing its performance in global searches.

A comprehensive landslide risk assessment is a necessary prerequisite for addressing the diverse and sensitive conditions in complex environments, aiming to effectively mitigate both existing and potential risks posed by landslide disasters. In landslide risk research, Sultana et al. [42] constructed a landslide susceptibility index, combining landslide-triggering factors and a comprehensive social vulnerability index to map landslide risk at a macro-scale in southeastern Bangladesh. Similarly, Chang et al. [43] developed a landslide susceptibility index and integrated hazard and vulnerability to conduct a comprehensive landslide risk assessment for Beiliu City in China. Additionally, Liu et al. [44] collected landslide susceptibility and social vulnerability factors to create a large-scale spatial distribution map of landslide risk across China. However, existing studies have yet to investigate the influence and patterns of landslide susceptibility evaluation results on the spatial distribution of landslide risk.

To address the aforementioned issues, this study proposes an integrated model combining XGBoost with the RIME optimization algorithm, along with a scientific landslide susceptibility evaluation system. The model effectively selects features and assigns weights by simulating the rime ice formation process, reducing complexity, improving prediction accuracy, and overcoming the overfitting problem faced by XGBoost in high-dimensional feature processing. Furthermore, the RIME model incorporates a hard fog penetration mechanism and a positive greedy algorithm, enhancing both the global search capability and convergence. This ensures a stable search process and improves the reliability of model parameters for the high-precision spatial prediction of landslide susceptibility. By integrating the concepts of landslide susceptibility, dynamic landslide factors, and social vulnerability, a comprehensive landslide risk index was developed for risk assessment. This study further investigates how landslide susceptibility results influence risk, identifying regions with varying levels of landslide risk due to spatial heterogeneity in the geological background, the natural environment, and socio-economic conditions. The main contributions of this study are as follows:

(1) Based on disaster risk theory and intelligent optimization algorithms, the RIME-XGBoost model is innovatively developed, significantly enhancing the accuracy of landslide susceptibility prediction, thus providing a solid data foundation for landslide risk assessment.
(2) A comprehensive landslide risk index is developed, facilitating the evaluation of regional landslide risk. This index identifies areas with varying levels of risk due to spatial heterogeneity in geological, geographical, and socio-economic conditions.
(3) This study investigates the mechanisms through which landslide susceptibility predictions influence landslide risk, offering robust theoretical support for disaster management agencies in formulating more precise and effective disaster prevention and mitigation measures.

2. Study Area and Dataset

2.1. Study Area

The study area is Wanzhou County in the Three Gorges Reservoir Area, which is located in the upper reaches of the Yangtze River and the northeastern part of the Chongqing municipality (Figure 1). This area is located at 107°55′22″E–108°53′25″E, 30°24′25″N–31°14′58″N, with an area of 3457 km^2. The region has a subtropical monsoon climate with four distinct seasons; it is humid and rainy, with rainfall generally concentrated from May to September [45]. The area has high and steep mountains, with large topographic undulations, and is eroded by the Yangtze River and its tributaries, which have formed a multilevel river-class geomorphology. The geological conditions are complex, and the strata mainly include Jurassic and Triassic sedimentary strata, mainly comprising the following: sandstone, mudstone, and shale; artificial accumulations; river alluvium; residual and slope deposits; and other widely distributed soil layers [46]. The rivers in this region are part of the Yangtze River system, featuring a well-developed water network with numerous tributaries, small streams, and ditches that create a complex surface runoff system.

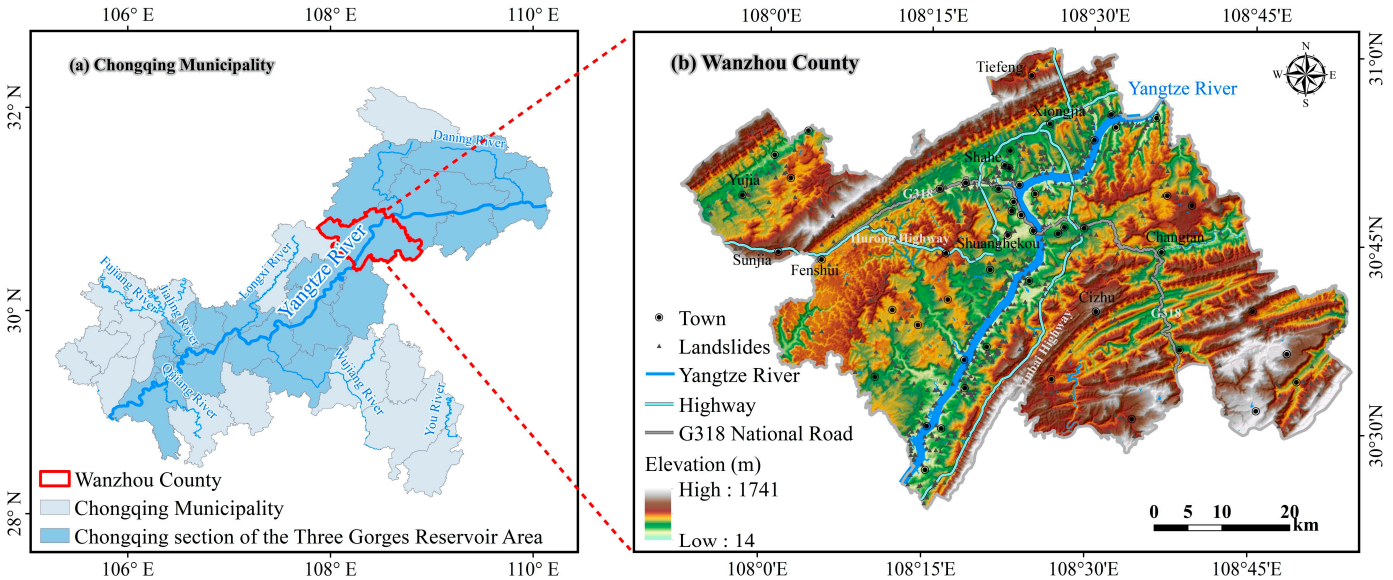


Figure 1. (**a**) Location of Wanzhou County in Chongqing Municipality; (**b**) elevation of Wanzhou County.

Wanzhou County, as a key area within the Three Gorges Reservoir Region, is characterized by a high density of geological disasters and a broad geographical distribution. The types of geological disasters in this region are diverse, primarily including landslides

and collapses, with landslides being particularly prominent and serving as a major factor affecting regional safety and stability. Table A1 illustrates several landslide events in Wanzhou County, revealing that these events are predominantly concentrated in July and August, a period marked by frequent heavy rainfall, which acts as a primary trigger for landslides. Given the extensive impacts of landslides, which can lead to severe damage to infrastructure such as houses and roads, as well as directly threatening human life and resulting in immeasurable economic and property losses, it is crucial to unveil the spatial distribution patterns of landslides and analyze their risks. This knowledge is of significant practical importance and scientific value for formulating disaster prevention and reduction strategies and mitigating the impacts of such disasters.

2.2. Data Collection and Preprocessing

2.2.1. Landslide Inventory Data

Landslide susceptibility maps cannot be developed without the basic support of landslide inventory data. Thus, reliable landslide inventory data are crucial for landslide studies [47–49]. In this study, we used the national spatial distribution data of geohazard points, which include a variety of geohazards, such as landslides, rockfall, debris flows, and ground fissures, released by the Resource and Environmental Science and Data Centre of the Chinese Academy of Sciences, to extract the landslide inventory data of the study area using ArcGIS 10.6 software.

In this study, a total of 709 landslide points were obtained (as shown in Figure 1b). Spatially, landslides are more common along the two sides of the Yangtze River. Statistically, the study area is dominated by small and medium landslides; most landslides are in "unstable" and "potentially unstable" states, so disaster prevention should be the continuous focus in this area.

Non-landslide points were generated at a ratio of 1:1, a practice that has been widely recognized in the field of landslide research [32,50,51]. In constructing the non-landslide sites, we carefully excluded the 1 km buffer zone of landslide sites and river areas to ensure that the data were pure and free from interference. Finally, we successfully constructed 709 non-landslide points, which, together with the original 709 landslide points, formed a sample set of 1418 data points. The data were divided into an 80% training set and a 20% test set for model training and prediction accuracy evaluation, respectively.

2.2.2. Landslide Susceptibility Assessment Data

Landslides are affected by a combination of internal geological conditions and external factors. Therefore, a reasonable selection of influencing factors is the key to assessing landslide susceptibility. However, a unified evaluation standard has not yet been established internationally. Lee et al. [52] classified these influencing factors into six categories—topography, hydrology, traffic, geology, soil, forest, and land use—through a big data mining analysis of 776 articles from 1999 to 2018. Reichenbach et al. [36] classified the factors influencing landslides into five categories: geology, hydrology, land cover, geomorphology, and other factors. Based on a literature review and regional data availability, we selected a total of 12 valid factors to assess landslide susceptibility in Wanzhou County. The spatial distribution of the data for all the landslide susceptibility assessment factors is shown in Figure 2.

Elevation plays a crucial role in landslide susceptibility assessment because it influences various factors, such as precipitation, topography, temperature, and soil moisture, thereby impacting landslide occurrence [53]. The slope, as a key element in determining the shear force of slopes, is an important and direct trigger of geological hazards [50]. The aspect influences precipitation, temperature, vegetation, and solar radiation, significantly

affecting the stability of geological formations [50]. North-facing slopes (in the Northern Hemisphere) that receive less solar radiation generally exhibit higher soil moisture and sparse vegetation levels, leading to lower soil stability and increased susceptibility to landslides. The plan curvature and profile curvature are also two key topographic factors in landslide susceptibility assessment [54]. Plan curvature reflects the shape and degree of surface relief and influences the convergence and dispersion of surface runoff. Profile curvature, on the other hand, plays an important role in the flow rate of surface material, which regulates the rate of movement and release of the energy of landslide material and rainfall runoff. The topographic wetness index (TWI) is a measure used to assess the influence of the terrain on water accumulation [55,56]. It is a combined measure of the slope and catchment area for estimating the moisture conditions at a particular location. Higher TWI values indicate areas more prone to water accumulation and greater soil instability.

Landslides usually occur under certain geological and environmental conditions. Lithology and faults are important geological indicators for landslide susceptibility assessment [57]. Lithology controls the development and evolution of landslides, and different types of rocks have significant effects on the slope soil type, slope structure, and soil shear strength. The study area is mainly composed of carbonate sedimentary rocks, mixed sedimentary rocks, and siliceous clastic sedimentary rocks. The more faults there are, the greater the probability of landslides.

The normalized difference vegetation index (NDVI) is widely used in the field of eco-geology. It is commonly employed to assess the vegetation coverage and indirectly reflects the soil moisture conditions. This index is based on Landsat 8 data and calculated via the Google Earth Engine cloud platform. In addition, the land cover reflects the degree of human interference and damage to rocks and soil [58]. The presence of forests helps to stabilize slopes, thus reducing the occurrence of landslides; however, the expansion of agricultural and residential land may destabilize slopes, thus triggering slope failures. Land use data were derived from the land use dataset produced by Yang et al. [59].

Wanzhou County has an abundance of water systems, and prolonged water erosion weakens soil stability, causing most landslide disasters to occur near these water systems. Road construction involves large-scale excavation and blasting, which can weaken the stability of geological formations and increase the likelihood of landslide disasters. Statistical analysis also indicates that the susceptibility to landslides increases with increasing distance from a road, especially within a certain range on either side of the road (e.g., within 500 m). Data on water systems and road networks are sourced from OpenStreetMap (OSM), and the distances to these water systems and roads are commonly selected indicators of landslide susceptibility.

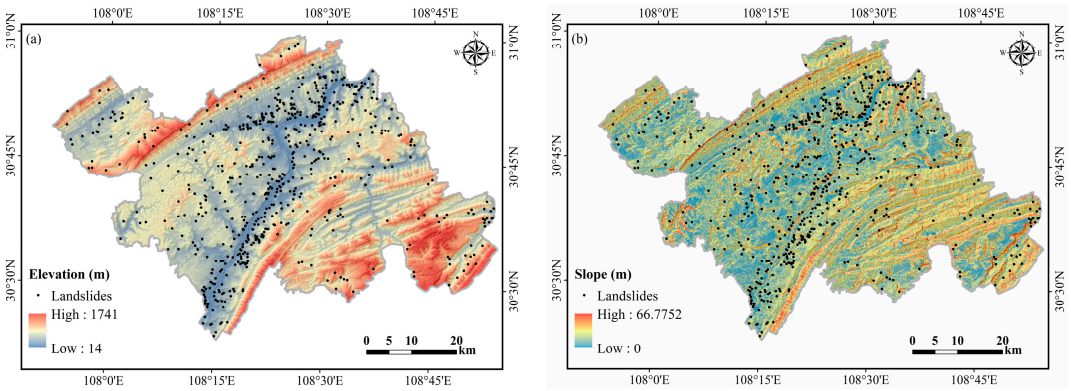


Figure 2. *Cont.*

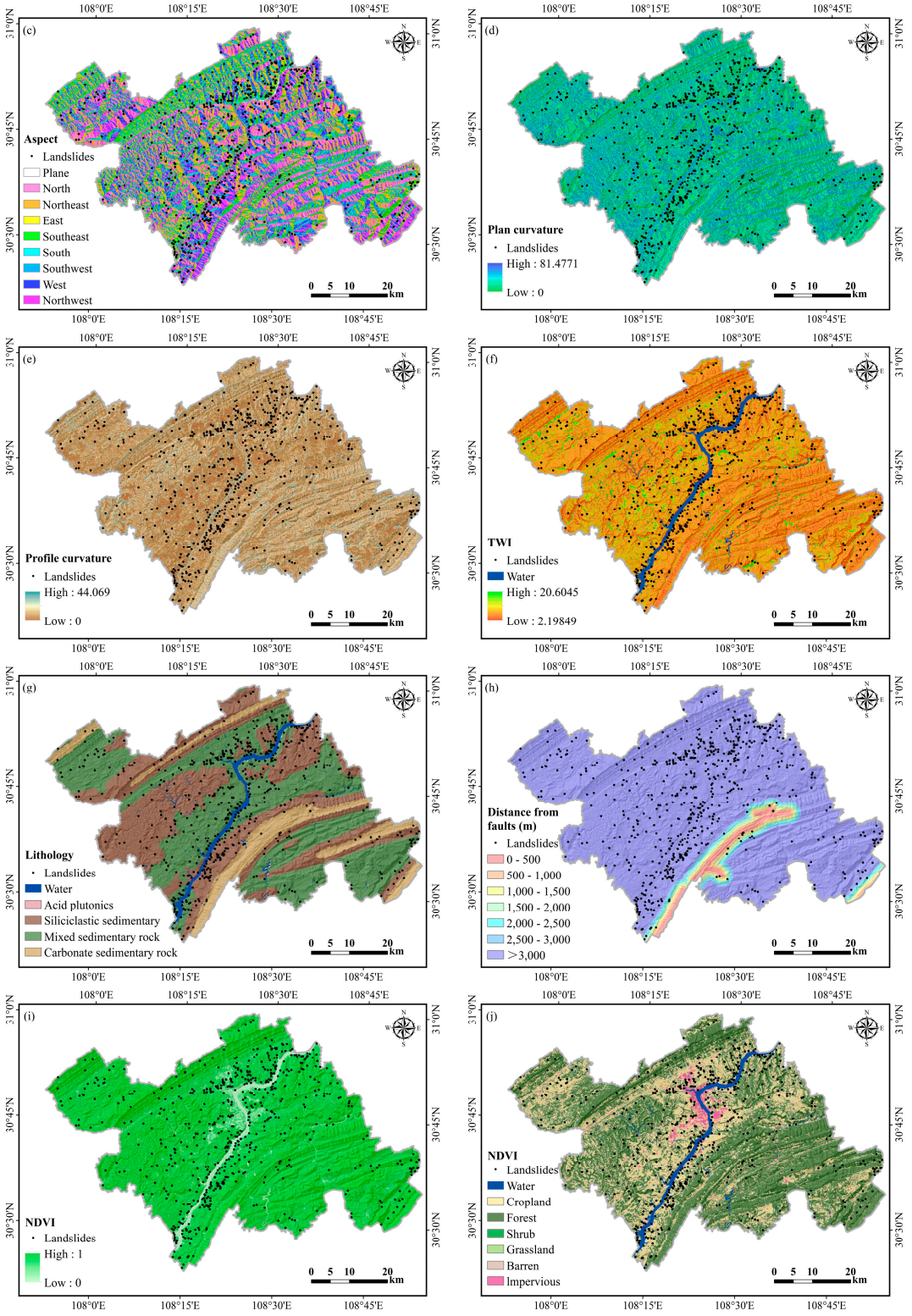


Figure 2. *Cont.*

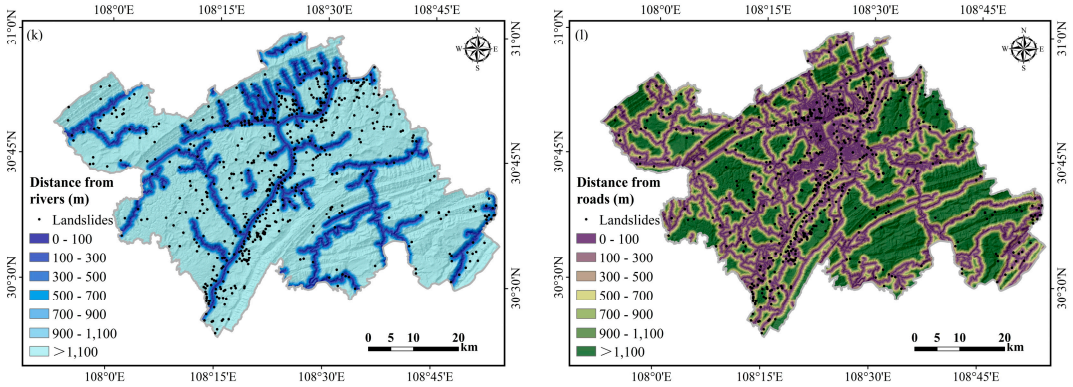


Figure 2. Factors influencing landslide susceptibility: (**a**) elevation; (**b**) slope; (**c**) aspect; (**d**) plan curvature; (**e**) profile curvature; (**f**) TWI; (**g**) lithology; (**h**) distance from faults; (**i**) NDVI; (**j**) land use; (**k**) distance from rivers; (**l**) distance from roads.

2.2.3. Landslide Hazard Assessment Data

In the field of landslide hazard assessment, a widely accepted unified computational paradigm is currently lacking. According to the authoritative definition of hazard by the United Nations, a comprehensive assessment of geological hazard must consider the probability of occurrence, the intensity of the disaster, and the potential impact range [60]. Given that historical records of geological disaster events are often incomplete, particularly concerning critical information such as timing, intensity, and scale, this situation poses significant challenges to the accuracy of assessment efforts [61,62]. As a result, in practical research and applications, scholars typically base their evaluations on landslide susceptibility assessment results, incorporating specific geological conditions to select various contributing factors for landslide hazards, aiming to achieve more accurate hazard assessments. This approach has gained widespread recognition and adoption in the international academic community [43,63,64].

For example, in the assessment of landslide hazards in karst topographic regions, researchers innovatively identified the soil erosion modulus as a key contributing factor, considering the significant slope instability caused by soil erosion in the area. They constructed a targeted hazard assessment model by integrating this factor with landslide susceptibility data [43]. Similarly, in Afghanistan, the research team selected surface runoff and glacier melt equivalents as core contributing factors, accounting for the melting of alpine snow and glacial water as the main triggers for landslides [64]. In the China–Pakistan Economic Corridor region, researchers have focused on the combination of rainfall erosion intensity and spatial susceptibility to provide a more comprehensive characterization of landslide hazards [63]. Notably, in assessing hazards in the northern mountain region of Pakistan, researchers have not only considered landslide susceptibility but also introduced two important factors, i.e., rainfall precipitation and peak ground acceleration, thereby enriching the dimensions of the assessment system [65]. Similarly, in the mining area of Guizhou, researchers have emphasized the importance of incorporating rainfall data of varying frequencies to increase the comprehensiveness and accuracy of disaster risk assessments [66]. Notably, Wanzhou County is a typical area prone to rainfall-induced landslides, and Xiao et al. [67] clearly indicate that more than 90% of landslide disasters in Wanzhou County are directly or indirectly related to rainfall, providing significant evidence for regional landslide hazard assessment. In light of this, this study innovatively proposes the combination of annual average rainfall and rainfall erosion intensity (which quantifies the potential impact of rainfall on soil erosion) as core contributing factors (Figure 3). By integrating these factors with landslide susceptibility assessment results, a landslide hazard index suitable for Wanzhou County is constructed. This approach incorporates

the region's unique meteorological conditions, expands upon existing assessment methods, and serves as an important reference for landslide hazard assessments in similar geological environments.

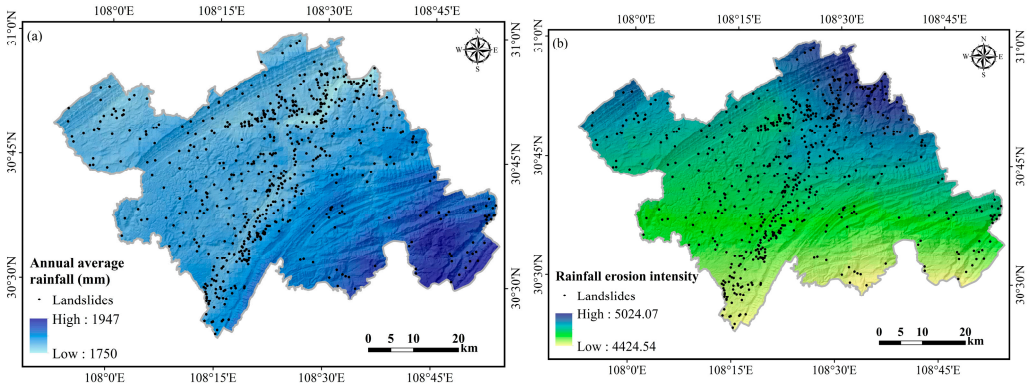


Figure 3. Hazard contributing factors for landslide hazards: (**a**) average annual rainfall; (**b**) rainfall erosion intensity.

The average annual rainfall was averaged over the period 2000–2020, reflecting the overall precipitation distribution in the region in a more stable way. The data were obtained from the National Tibetan Plateau Scientific Data Centre, with a resolution of 1 km and a resampling process of 30 m [68]. The rainfall erosion intensity data are derived from the data product of Yue et al., which has undergone rigorous cross-validation, ensuring a high level of accuracy [69].

2.2.4. Landslide Vulnerability Assessment Data

Disaster vulnerability assessment is an essential component of geological disaster risk management, and its importance is increasingly highlighted in geological disaster scientific research. The United Nations Office for Disaster Risk Reduction authoritatively defines the concept of vulnerability, expanding it to encompass various dimensions, including material, population, environmental, economic, and social aspects, as well as the system's capacity to withstand risks [70]. Given the complex and variable nature of disasters and the heterogeneity of the natural and social environments of disaster-prone entities, there is currently a lack of universally applicable standardized evaluation indicators for vulnerability assessment. Researchers evaluate landslide vulnerability for specific elements (such as roads [71] and buildings [72,73]) or conduct comprehensive regional vulnerability assessments [43,64] by analyzing the interaction mechanisms between geological hazards and the surrounding environment.

This study establishes a scientifically sound vulnerability assessment indicator system for landslide disasters, aiming to comprehensively evaluate the impact of such disasters on vulnerable entities. The system is meticulously designed to account for potential losses of various vulnerable entities and the accessibility of assessment factors, covering three core dimensions of vulnerability: population, economy, and material. Specifically, population vulnerability focuses on the potential risk of casualties from disasters, emphasizing the susceptibility of densely populated areas and the limitations faced by vulnerable groups, such as the elderly and children, in terms of self-rescue capabilities, mobility, and disaster awareness. Consequently, this study selects population density, individuals aged 65 and older, and children under 5 as key indicators of population vulnerability. Economic vulnerability focuses on the potential impacts of disaster events on regional economic structures, using Gross Domestic Product (GDP) as a core metric. As a key indicator of economic activity, GDP represents the total value of goods and services produced within a region

over a specified time period. Incorporating GDP into the analytical framework allows for an effective assessment of the intrinsic relationship between the regional economic scale and its exposure to disaster risk. Moreover, material vulnerability concentrates on the direct destruction of residents' essential infrastructure by disasters. This study employs three specific indicators—POI (point of interest) density, building density, and road density—to comprehensively assess the impact of geological disasters on the integrity and functional recovery capacity of regional infrastructure networks. In summary, the landslide vulnerability assessment indicator system developed in this study not only deepens the understanding of the multidimensional characteristics of geological disaster vulnerability but also provides a solid scientific basis for formulating precise and effective disaster prevention and reduction strategies.

We obtained POI data for schools, shops, restaurants, parks, hospitals, etc., via Python. The road data were obtained from the OSM and processed via ArcGIS to calculate the road network density. The building data were obtained from the first national land-cover dataset (SinoLC-1), with a resolution of 1 m [74]. The GDP data were obtained from the Resource and Environmental Science Data Centre at a resolution of 1 km, which was upgraded to 30 m by resampling to match the resolutions of the other data. The population-related data are sourced from WorldPop. The vulnerability indicator layer datasets are shown in Figure 4. Detailed information about all the data is presented in Table 1.

Table 1. The sources and details of multi-source indicator data for landslide risk assessment.

Factor	Data Type	Data Source	Resolution/Scale
Elevation	Raster	National Aeronautics and Space Administration (https://earthdata.nasa.gov/) (accessed on 1 May 2024)	30 m
Slope			
Aspect			
Plan curvature			
Profile curvature			
TWI			
Lithology	Raster	A new database of global lithological maps [75] (https://zenodo.org/record/1464846) (accessed on 1 May 2024)	250 m
Distance from faults	Vector	National 1:200,000 geological map spatial database (https://geocloud.cgs.gov.cn/) (accessed on 1 May 2024)	1:200,000
NDVI	Raster	Google Earth Engine (https://developers.google.cn/earth-engine) (accessed on 20 May 2024)	30 m
Land use	Raster	The 30 m annual land-cover datasets [59] (https://zenodo.org/records/8176941) (accessed on 1 May 2024)	30 m
Distance from rivers	Vector	OpenStreetMap (https://download.geofabrik.de/asia/china.html) (accessed on 1 May 2024)	——
Distance from roads			
Building density	Raster	The first 1 m resolution national-scale land-cover map of China [74] (https://zenodo.org/records/8214467) (accessed on 20 May 2024)	1 m
Annual average rainfall	Raster	National Tibetan Plateau Science Data Centre (https://data.tpdc.ac.cn/home) (accessed on 20 May 2024)	1 km
Rainfall erosivity intensity	Raster	https://dx.doi.org/10.12275/bnu.clicia.rainfallerosivity.CN.001 [69] (accessed on 20 May 2024)	1 km
POI	Vector	Web crawler	——
Population	Raster	WorldPop	100 m
GDP	Raster	Resource and Environmental Sciences Data Centre (https://www.resdc.cn/) (accessed on 20 May 2024)	1 km
Road density	Vector	OpenStreetMap (https://download.geofabrik.de/asia/china.html) (accessed on 1 May 2024)	——
Building density	Raster	The first 1 m resolution national-scale land-cover map of China [74] (https://zenodo.org/records/8214467) (accessed on 20 May 2024)	1 m

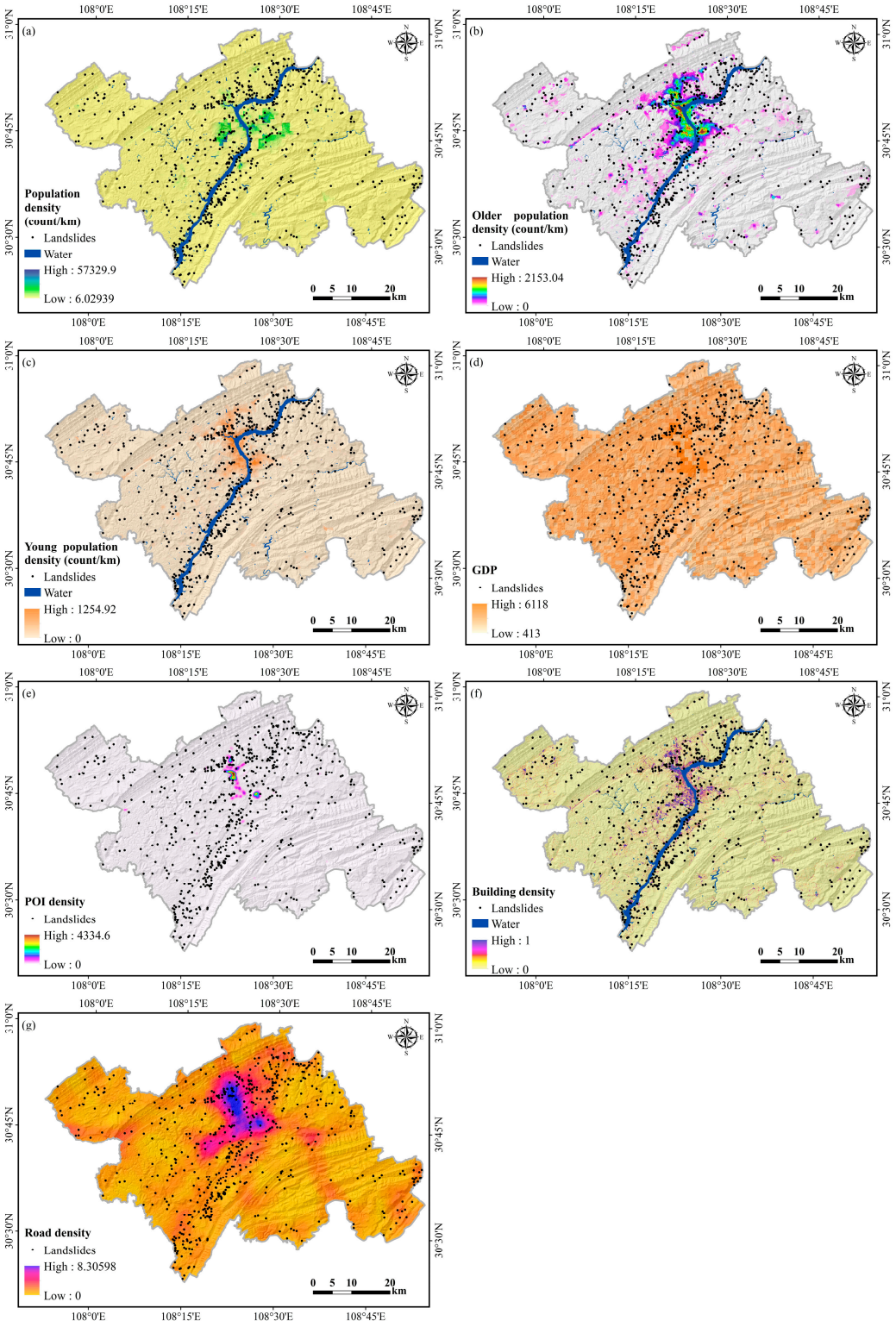
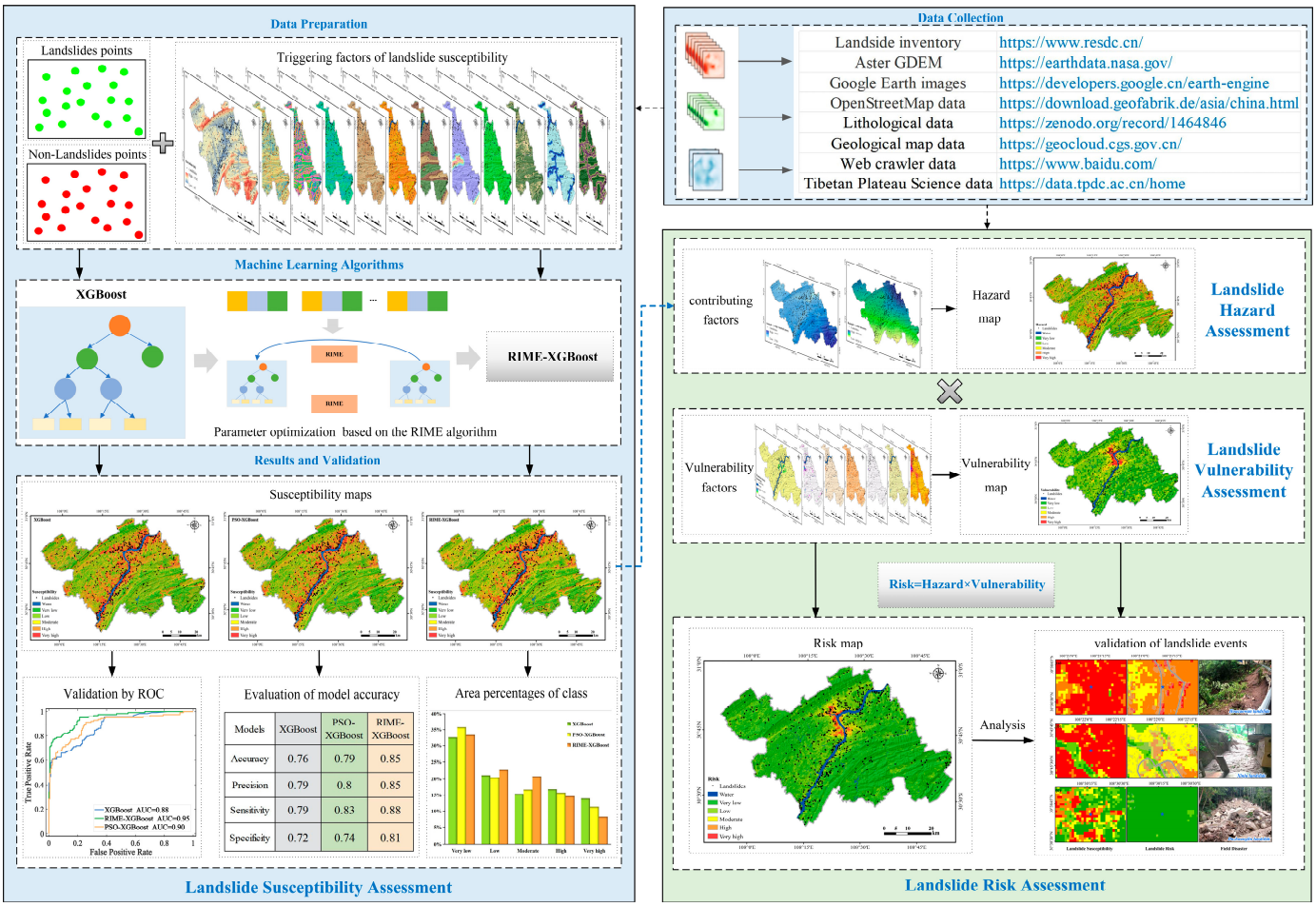


Figure 4. Factors influencing landslide vulnerability: (**a**) population density; (**b**) older population density; (**c**) young population density; (**d**) GDP; (**e**) POI density, (**f**) building density; (**g**) road density.

3. Integrated Landslide Risk Assessment Methods

In the complex process of landslide risk assessment, diverse influencing factors are flexibly and precisely selected based on the region's unique geological environmental characteristics and the multidimensional traits of disaster-prone entities to construct a scientifically robust evaluation system. This study develops an indicator system and

methodological model for landslide risk assessment in Wanzhou County, as outlined below (Figure 5): (1) Landslide susceptibility assessment: Using landslide point data and a comprehensive dataset of influencing factors, the RIME-XGBoost model is innovatively employed to assess landslide susceptibility in Wanzhou County. To validate the model's effectiveness and superiority, comparative analyses with the XGBoost, PSO-XGBoost, RF, support vector regression (SVR), and convolutional bidirectional long short-term memory neural network (CNN-BiLSTM) models are conducted for susceptibility assessment. This process optimizes and supplements current susceptibility prediction models, laying a solid and precise data foundation for subsequent risk evaluation work. (2) Landslide risk assessment: Building upon the reliable results of the landslide susceptibility assessment, we further integrate the contributing factors of landslide hazards through complex and detailed analyses to derive the landslide hazard index. On the basis of the meticulously constructed multidimensional vulnerability evaluation indicator system for disaster-prone entities, a systematic analysis of the potential disaster situations for different entities under landslide threats is subsequently conducted, resulting in a comprehensive vulnerability index that reflects the susceptibility of regional disaster-prone entities. Finally, through a scientifically rigorous integration method, the hazard index and vulnerability index are closely combined to calculate the landslide risk index, providing a strong scientific basis for the prevention and management of landslide disasters in Wanzhou County.



Models	XGBoost	PSO-XGBoost	RIME-XGBoost
Accuracy	0.76	0.79	0.85
Precision	0.79	0.8	0.85
Sensitivity	0.79	0.83	0.88
Specificity	0.72	0.74	0.81

Figure 5. Flowchart of this study.

3.1. Landslide Risk Assessment Model

3.1.1. Hazard

On the basis of the description in Section 2.2.3, where the region is characterized primarily by rainfall-induced landslides, this study selects rainfall erosion intensity and annual average rainfall as contributing factors for landslide hazard. Together with landslide susceptibility, hazards are assessed according to Formula (1).

$$Hazard = Susceptibility \times (T_1 + T_2) \quad (1)$$

where T_1 denotes the annual average rainfall and where T_2 denotes the rainfall erosion intensity.

3.1.2. Vulnerability

As elaborated in Section 2.2.4, we systematically and thoroughly analyze the multidimensional disaster-prone entities potentially affected by mountain landslides and their complex impacts. Given the current situation in Wanzhou County, where the urban population is dense and the economy is prosperous, while the vulnerability to disasters is significantly heightened, we constructed a robust comprehensive evaluation indicator system for geological disaster vulnerability. This system accounts for the specific availability and relevance of assessment factors within the study area. This assessment system focuses on three key dimensions of vulnerability: population, economy, and material. Through a comprehensive and in-depth analysis, the integrated vulnerability characteristics of disaster-prone areas from multiple dimensions are presented. For the population vulnerability assessment, indicators such as population density, the elderly population, and the young population are selected to accurately reflect the sensitivity and vulnerability of the social structure. In terms of economic vulnerability, GDP is used as a measurement standard to intuitively display the potential economic losses in a region during disaster events. In the assessment of material vulnerability, we have chosen commonly used indicators such as building density and road density and innovatively incorporated the density of points of interest (POIs), which reflects various points, including hospitals, schools, restaurants, shopping malls, and parks. A higher density of POIs indicates a greater potential threat to the region and higher vulnerability. After a detailed analysis of the vulnerability of various factors, a scientific synthesis of the different categories of disaster-prone entities exposed to hazards is conducted, leading to a comprehensive vulnerability assessment result. The vulnerability formula is as follows:

$$Vulnerability = \frac{1}{3}V_P + \frac{1}{3}V_E + \frac{1}{3}V_M \quad (2)$$

The overall vulnerability consists of three components: population vulnerability (V_P), economic vulnerability (V_E), and material vulnerability (V_M). Given that the importance of assessing the vulnerability of disaster-affected entities cannot be clearly distinguished, we do not differentiate their significance here; therefore, equal weights are applied in the formula.

3.1.3. Risk

The risk assessment model primarily includes the assessment of hazard and vulnerability (Formula (3)) [43,63,64]. Hazards portray the natural attributes of landslides, whereas vulnerability reveals the impact of landslides on the social dimension. The formula for landslide risk is as follows:

$$Risk = Hazard \times Vulnerability \quad (3)$$

3.2. RIME-XGBoost Landslide Susceptibility Assessment Model

3.2.1. XGBoost Model

XGBoost is a machine learning algorithm developed from the gradient boosting decision tree (GBDT) algorithm that incorporates gradient information on the basis of integrated learning to optimize an objective function and obtain the optimal solution [76]. In comparison to GBDT, the XGBoost algorithm can utilize the first-order derivative of the loss function to achieve a Taylor expansion and obtain the second-order derivative, resulting in a faster optimal solution.

$$\hat{y}_i = \sum_{n=1}^{N} f_n(x_i), f_n \in FS \tag{4}$$

where the forest set FS is the set of decision trees; x_i is the vector of eigenvalues for the $i-th$ data point; $f_n(x_i)$ is the $n-th$ independent decision tree, which has a tree structure and is associated with weight information; N is the total number of decision trees; and $\hat{y}_i$ is the predicted value for the $i-th$ data point.

XGBoost obtains the optimal solution through multiple iterations, where the loss function for round t can be expressed as shown in Equation (5).

$$Loss^{(t)} = \sum_{i=1}^{M} L(y_i, \hat{y}_i) + \sum_{n=1}^{N} \Omega(f_n) \tag{5}$$

By setting the number of iterations and the structural information for the decision tree, we can obtain a trained XGBoost model $\sum_{n=1}^{N} f_n(x_i), f_n \in FS$ for a given dataset.

3.2.2. XGBoost Model Based on RIME Optimization

XGBoost can be affected by initial features such as the initial weights, the number of iterations, and the learning rate, resulting in suboptimal prediction learning effects. Therefore, in this study, an XGBoost prediction model based on RIME optimization is designed to enhance the learning state of the stable XGBoost approach. RIME is a soft mist search strategy based on the movement of soft mist particles [41]. The soft fog search process is susceptible to information exchange, which affects the optimal solution. Therefore, to improve the search efficiency and solution accuracy of the model, a mechanism similar to that of the hard fog penetration method is applied to achieve dimensional crisscrossing and exchange between ordinary and optimal agents. In addition, an improved positive greedy selection mechanism is adopted on the basis of the original greedy selection mechanism. This improvement enhances the diversity of the population by altering the process of selecting the best solution, thereby maximizing the avoidance of the algorithm falling into a locally optimal state. The entire algorithm's procedure is illustrated in Figure 6.

In this paper, the feature parameter x_i to be optimized in the XGBoost algorithm is set to search for a RIME agent, and all real-time composite data proxies are considered. First, the whole RIME population Q is initialized. As shown in Equation (6), the RIME population consists of n RIME agents S_i, and each RIME agent consists of d RIME particles x_{ij}. Therefore, as shown in Equation (7), the Q population can be directly represented by RIME particles.

$$Q = \begin{bmatrix} S_1 \\ S_2 \\ \vdots \\ S_i \end{bmatrix}; S_i = \begin{bmatrix} x_{i1} & x_{i2} & \cdots & x_{ij} \end{bmatrix} \tag{6}$$

$$Q = \begin{bmatrix} x_{11} & x_{12} & \cdots & x_{1j} \\ x_{21} & x_{22} & \cdots & x_{2j} \\ \vdots & \vdots & \vdots & \vdots \\ x_{i1} & x_{i2} & \cdots & x_{ij} \end{bmatrix} \tag{7}$$

where i is the serial number of a RIME agent and j is the serial number of a RIME particle.

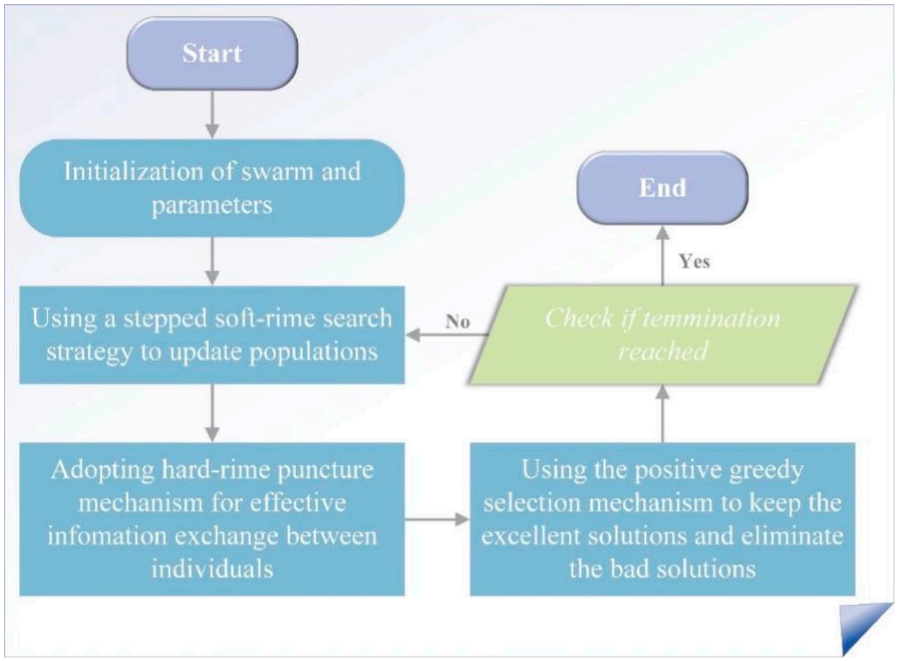


Figure 6. Structure of the RIME algorithm.

RIME is used to determine the positions of the fog particles and their soft fog particle motion characteristics, as shown in Equation (8).

$$Q_{ij}^{new} = Q_{best.j} + r_1 \cdot \cos\theta \cdot \beta \cdot (h \cdot (Ub_{ij} - Lb_{ij}) + Lb_{ij}), r_2 < E \tag{8}$$

where Q_{ij}^{new} is the new position of the corresponding particle after the update. $Q_{best.j}$ is the $j-th$ particle associated with the best RIME agent in population Q. Ub_{ij} and Lb_{ij} represent the upper and lower limits of the escape space, respectively. These bounds delineate the effective region within which particle motion is constrained. Q_j controls the motion direction of the particles, and $\cos\theta$ varies with the number of iterations. The parameter r is a random number within the range $(-1, 1)$. Factor β is an environmental element that ensures algorithm convergence. h is the degree of adhesion, which is a random number within the range $(0, 1)$ that controls the distance between the centers of two RIME particles. Moreover, $\theta = \pi \cdot \frac{t}{10 \cdot T}$, $\beta = 1 - \left[\frac{w \cdot t}{T}\right]/w$, and $E = \sqrt{t/T}$.

To better update the agents of the algorithms so that the particles in the algorithms can be exchanged and the algorithms can converge and avoid local optima, we introduce a hard-RIME puncture mechanism based on the soft-RIME search strategy.

$$Q_{ij}^{new} = Q_{best,j}, r_3 < F^{normr}(S_i) \tag{9}$$

$F^{normr}(S_i)$ denotes the normalized fitness value of the current agent and represents the probability of the $i-th$ RIME agent being selected.

Finally, the population is updated using a positive greedy algorithm. The algorithmic flowchart of the update process is as follows in Algorithm 1.

Algorithm 1. Pseudocode of the positive greedy selection mechanism

Initialize the RIME population Q
Obtain the current optimal agent and fitness value
While $t \leq T$
For $i = 1 : n$
If $F(Q_i^{new}) < F(Q_i)$
$F(Q_i) = F(Q_i^{new})$
$Q_i = Q_i^{new}$
If $F(Q_i^{new}) < F(Q_{best})$
$F(Q_{best}) = F(Q_i^{new})$
$Q_{best} = Q_i^{new}$
End If
End If
End For
$t = t + 1$
End While

3.2.3. Model Accuracy Evaluation

A confusion matrix is a matrix representation used to measure the performance of classification models. The accuracy, precision, sensitivity, specificity, and F1 score calculated from the confusion matrix provide a comprehensive overview of the performance of a classification model.

The accuracy of the model was evaluated by generating receiver operating characteristic (ROC) curves [77] and calculating the area under the curve (AUC). The closer the AUC is to 1, the higher the model's classification accuracy.

4. Results

4.1. Landslide Susceptibility Assessment Results

4.1.1. Landslide Factor Selection

Factor independence is crucial for model assessment. Multiple covariances interfere with the ability of a model to distinguish the effects of independent variables on dependent variables, leading to uneven weight distributions, increased interpretation complexity, and reduced prediction accuracy. Figure 7 shows that among the 12 initial factors, elevation had the highest correlation coefficient with river distance (0.47), but the correlation coefficients among all the factors were lower than 0.5, indicating no significant correlation. The multicollinearity test (Table 2) showed that the variance inflation factor (VIF) values of all moderating factors were <2 and that the tolerance (TOL) values were >0.1, indicating no multicollinearity. Therefore, all 12 factors were selected in this study.

Table 2. Multicollinearity check of environmental factors.

Number	Factor	Collinearity Statistic	
		Tolerance	VIF
1	Elevation	0.685	1.461
2	Slope	0.576	1.735
3	Aspect	0.981	1.019
4	Plan curvature	0.747	1.338
5	Profile curvature	0.857	1.168
6	TWI	0.668	1.497
7	Lithology	0.927	1.078
8	Distance from faults	0.939	1.065
9	NDVI	0.627	1.594
10	Land use	0.823	1.215
11	Distance from rivers	0.761	1.315
12	Distance from roads	0.794	1.337

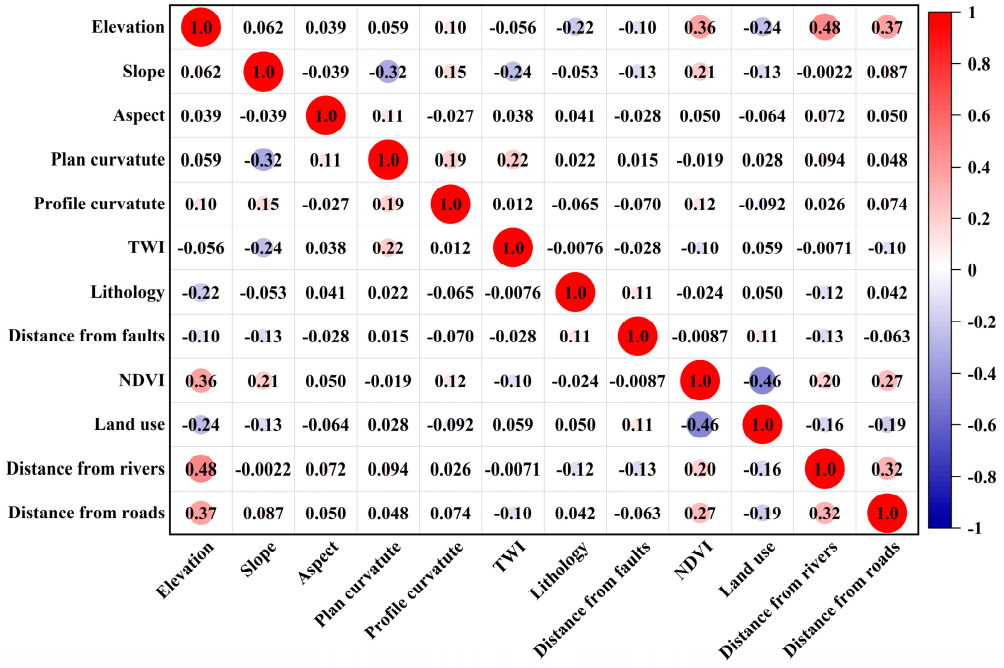


Figure 7. Pearson correlation coefficient plot.

4.1.2. Relationships Between Landslides and Various Influencing Factors

We used the nonparametric kernel density method to accurately depict the probability density distribution of landslide hazard points for each continuous variable and visualized the distribution of the number of landslide hazard points in different categorical variables through histograms. These graphical analyses provide strong support for an in-depth understanding of the complex relationships between landslides and various potential influencing factors.

Figure 8 reveals that the occurrence of landslides is significantly greater in the range of 100 to 500 m above sea level. Landslides are distributed mainly near slopes with gradients ranging from 10° to 25°, while steep slopes have relatively low landslide susceptibility. The effect of aspect on the distribution of landslides was not significant. In terms of plan curvature and profile curvature, low-level values were found to be more favorable for landslides. These findings reveal the key role of topographic and geomorphological features in landslide formation.

In addition, the closer an area is to a river, the greater the probability of landslide occurrence, which may be closely related to hydrogeological conditions. Landslides typically occur near roads, reflecting how human engineering activities can alter geological conditions, leading to slope instability. Moreover, the occurrence of these landslides poses a significant threat to roads, resulting in substantial damage. Landslide disasters are also more frequent in areas with greater vegetation cover, especially in intervals where the NDVI is in the range of 0.85 to 0.95. In terms of geological lithology, mixed sedimentary rocks and siliceous clastic sedimentary rocks are the main lithological types of landslide disasters, leading to 388 and 291 landslides, respectively. By analyzing these influencing factors in depth, the relationships between the occurrence of landslides and the natural and geological base environments can be further clarified.

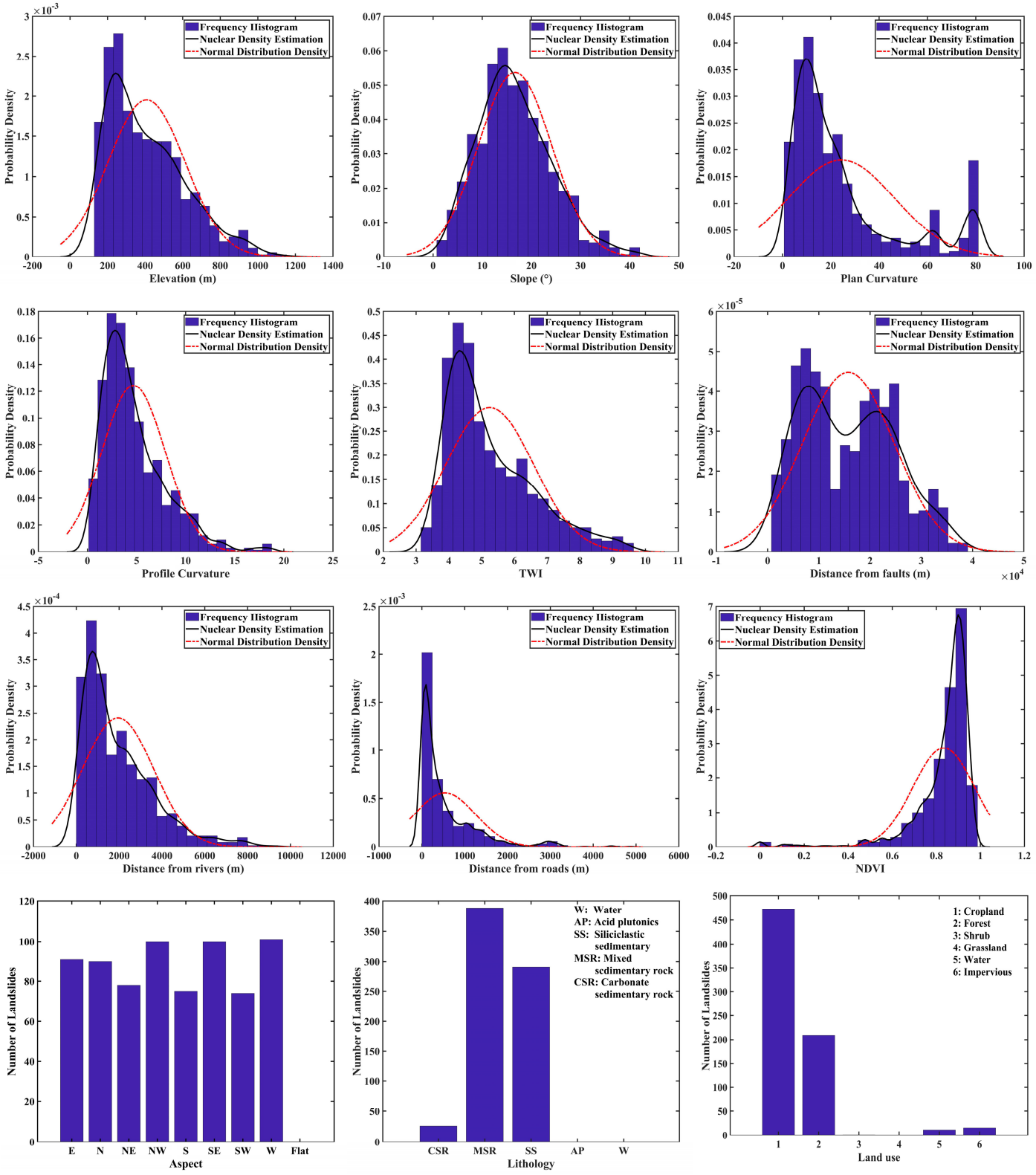


Figure 8. Relationships between landslides and various influencing factors.

4.1.3. Performance Evaluation of Landslide Susceptibility Models

(1) Optimization of model parameters

The performances of two models based on the XGBoost algorithm (the RIME-XGBoost and PSO-XGBoost models) with optimized parameters were compared during training by loss curve graph analysis. The loss curve of the RIME-XGBoost model quickly converges to

a lower level during the early stage of training, and the overall change is smooth, indicating that the model can quickly converge to a better solution and is stable during training (Figure 9). In contrast, the loss curve of the PSO-XGBoost model, although eventually stabilizing at a similar level, fluctuates more during the process, implying that the model is unstable during parameter or structure adjustment, which may affect its generalizability and prediction reliability. Therefore, in terms of loss values and curve smoothness, the RIME-XGBoost model achieves better performance and is superior in terms of prediction accuracy and stability. The performance of the PSO-XGBoost model is similar, but further optimization is needed to enhance its training stability.

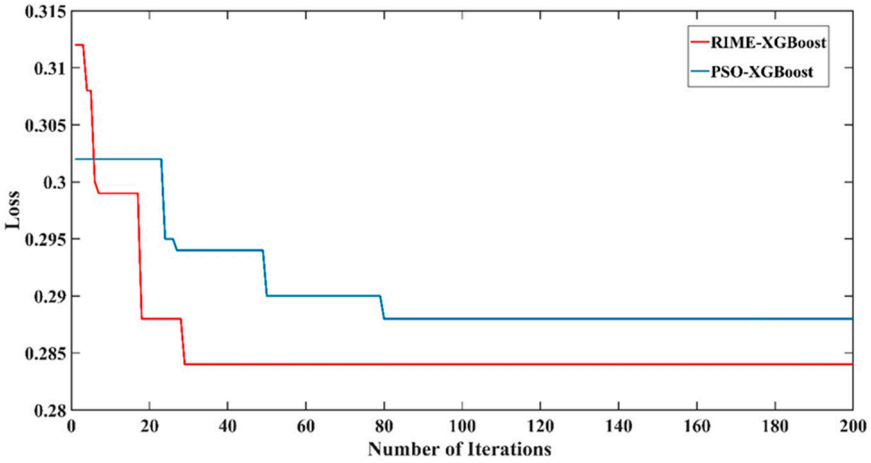


Figure 9. Loss curves for different models.

(2) Confusion matrix

In the fine-grained model evaluation considerations, we aim to fully examine the performance of the models through a series of key metrics (Table 3). Detailed observations indicate that the single XGBoost model performed well across various metrics, achieving an accuracy of 0.76, along with precision and sensitivity values of 0.79, a specificity of 0.72, and an F1 score of 0.79. For a more comprehensive comparison with the XGBoost model, this study selected other representative models for comparison. Notably, the deep learning models CNN-BiLSTM demonstrated an accuracy equivalent to XGBoost, whereas their specificity was superior by 0.09. However, their precision, sensitivity, and F1 scores lagged significantly behind those of the XGBoost model. In comparison with support vector regression (SVR) and classic classification algorithms like random forests (RF), XGBoost clearly outperformed these alternatives. The optimized PSO-XGBoost model showed slight improvements across all metrics, confirming the effectiveness of the optimization algorithm. The most impressive model, however, was the RIME-XGBoost model, which significantly outperformed all other models across all performance indicators. Its accuracy reached 0.85, with precision and sensitivity improving to 0.85 and 0.88, respectively, while specificity increased to 0.81 and the F1 score to 0.86. These results demonstrate that the RIME-XGBoost model possesses strong classification capabilities and notable robustness in predicting landslide susceptibility.

Table 3. Model performance.

Model	Accuracy	Precision	Sensitivity	Specificity	F1 Score
XGBoost	0.76	0.79	0.79	0.72	0.79
PSO-XGBoost	0.79	0.80	0.83	0.74	0.81
RIME-XGBoost	0.85	0.85	0.88	0.81	0.86
SVR	0.70	0.75	0.48	0.70	0.59
CNN-BiLSTM	0.76	0.76	0.76	0.81	0.72
RF	0.72	0.75	0.56	0.75	0.65

(3) ROC curve

The ROC curve and its AUC score are also key metrics for evaluating model performance (as shown in Figure 10). The original XGBoost model achieved an AUC of 0.88, while the AUC of the CNN-BiLSTM model was comparable to that of XGBoost, demonstrating satisfactory performance. The AUCs for the SVR and RF models were somewhat lower. However, the PSO-XGBoost model exhibited a slight improvement, with an AUC of 0.90. Notably, the RIME-XGBoost model significantly outperformed all other models, attaining an AUC of 0.95. This underscores its high accuracy and low false-positive rate in sample identification, thereby validating the effectiveness of the RIME optimization strategy.

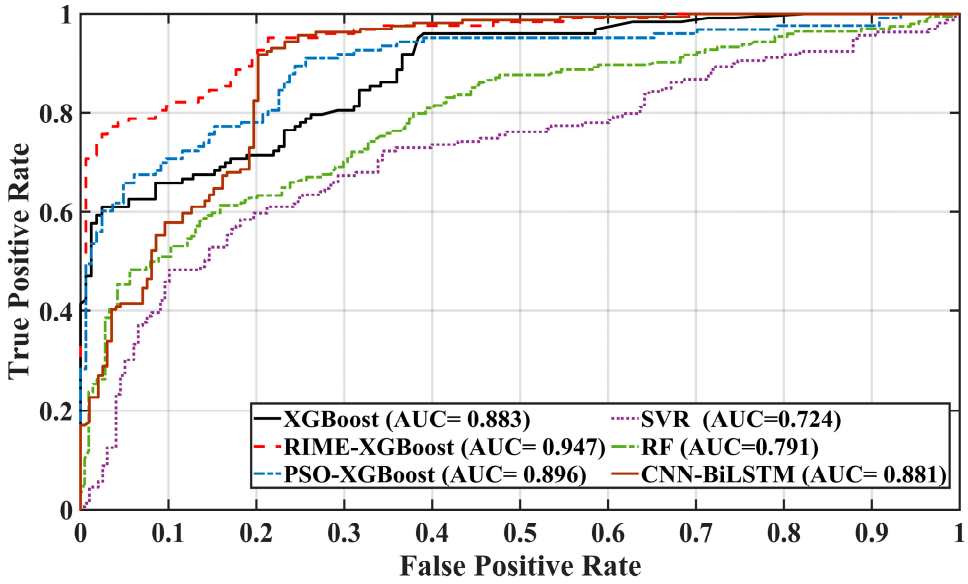


Figure 10. ROC curves plotted using test set data.

(4) Uncertainty analysis based on the cloud theory

Additionally, to further assess the model's performance, a cloud model was selected to analyze the prediction results (supported by our previous theoretical foundation and work) [78–80], as shown in Table 4. The analysis is conducted from three perspectives:

(1) Expectation E_x refers to the overall expectation within the region, generally described using the sample mean.

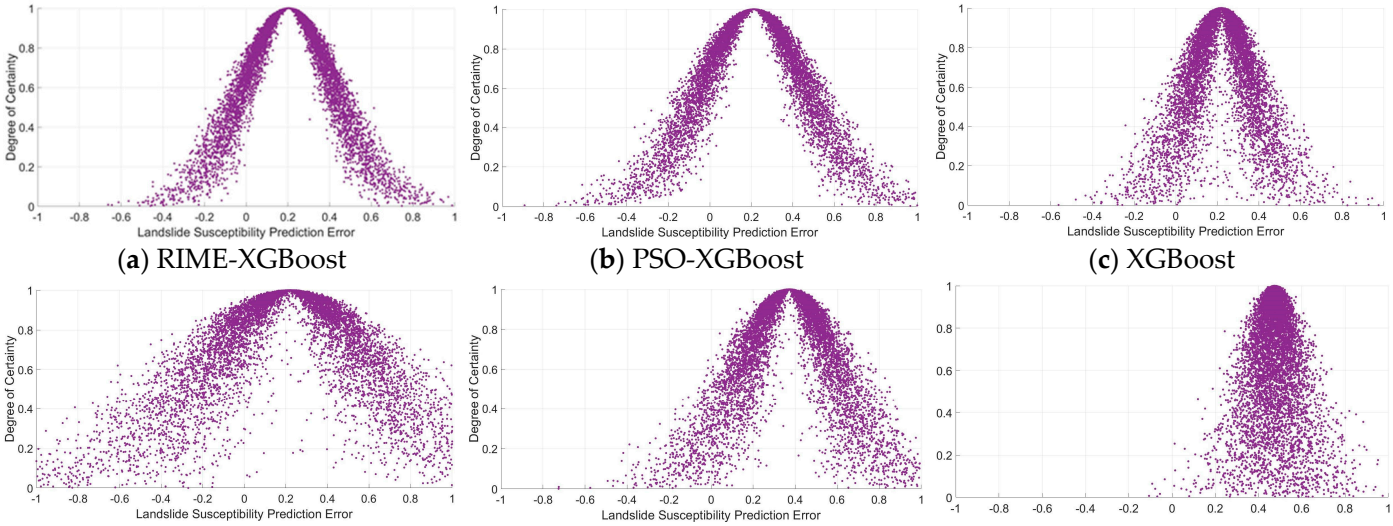
(2) Entropy E_n is an indicator used to comprehensively measure the fuzzy degree of qualitative concepts and probabilities, i.e., randomness. In the text, it mainly reflects the fluctuation range of the errors within the model forecasting range.

(3) Super-entropy H_e describes the uncertainty of entropy E_n, and its numerical value indicates the degree of data dispersion. The greater the value, the greater the degree of dispersion. In the text, it mainly reflects the frequency of error fluctuations within the model forecasting range.

Table 4. Formula of the cloud model.

Nature	Formula
Expectation E_x	$E_x = \frac{1}{N}\sum_{i=1}^{N} X_i$
Entropy E_n	$E_n = \sqrt{\frac{\pi}{2}} \times \frac{1}{N}\sum_{i=1}^{N}\left\|x_i - E_x\right\|$
Super-entropy H_e	$S^2 = \frac{1}{N-1}\sum_{i=1}^{N}(x_i - E_x)^2$ $H_e = \sqrt{S^2 - E_n^2}$

As illustrated in Figure 11 and Table 5, the expectation and hyper-entropy of the prediction errors using RIME-XGBoost are at their minimum, and the expected value of XGBoost is lower than that of SVR, CNN-BiLSTM, and RF, indicating a higher predictive accuracy for XGBoost. CNN-BiLSTM ranks second, showing only a slight performance gap compared to XGBoost.



(**a**) RIME-XGBoost (**b**) PSO-XGBoost (**c**) XGBoost

(**d**) CNN-BiLSTM (**e**) RF (**f**) SVR

Figure 11. Landslide susceptibility prediction error cloud map.

Table 5. Landslide susceptibility prediction error cloud model.

Model	Ex	En	He
XGBoost	0.2196	0.1451	0.0534
PSO-XGBoost	0.2129	0.2521	0.0466
RIME-XGBoost	0.2031	0.2171	0.0357
SVR	0.4742	0.0602	0.0661
CNN-BiLSTM	0.2207	0.3931	0.1305
RF	0.3728	0.2196	0.0644

Regarding the entropy (En), SVR exhibited the lowest values across all models. This can be attributed to the fact that entropy represents a range of error fluctuations, and since the predicted probabilities for SVR predominantly fall within the 0.3–0.7 interval, the fluctuation range is limited. In contrast, CNN-BiLSTM performs relatively well in this aspect due to its deep learning characteristics, which tend to skew its predictions towards probability extremes, potentially resulting in larger errors when predictions are incorrect.

In terms of hyper-entropy (He), it is evident that the standalone XGBoost model has a smaller value compared to other single models, indicating lower fluctuation frequency and stronger stability, whereas CNN-BiLSTM performs poorly in this regard.

Figure 11 also presents the predicted error cloud map for landslide susceptibility, showing that RIME-XGBoost has the most favorable cloud drop distribution, while SVR is the most scattered. Among the individual models, XGBoost's distribution is the most reasonable. Additionally, corresponding to Table 5, we can conclude the following: 1. Entropy reflects the concentration of the probability density distribution of landslide susceptibility predictions. A larger entropy value leads to a clearer shape of the distribution curve. As the distribution becomes sharper, the uncertainty decreases, resulting in greater stability. 2. A decreasing hyper-entropy indicates an increase in the cohesiveness of the distribution curve. The predictive error between actual outputs and predicted values is minimal, and these errors display lower volatility.

Through the qualitative and quantitative uncertainty analysis of the landslide susceptibility prediction models, we can determine that the standalone XGBoost model demonstrates greater stability in predicting landslide susceptibility. The performance of the XGBoost model, optimized through RIME, is the best and most stable.

4.1.4. Mapping of the Landslide Susceptibility with the Different Models

After training and testing the model with 12 key landslide-controlling factors, the regional landslide susceptibility index (LSI) was calculated and mapped in ArcGIS (Figure 12). Based on LSI values from the XGBoost model, the natural break method classified the results into five susceptibility levels: very low (<0.173), low (0.173–0.365), moderate (0.365–0.565), high (0.565–0.785), and very high (>0.785). The same classification thresholds were applied to the results of other models. The spatial distribution patterns were highly consistent across all models, confirming their reliability. Moreover, the high- and very-high-susceptibility zones closely aligned with actual landslide occurrences (Table A2), highlighting the accuracy of the predictions.

The southwestern and northeastern regions exhibit elevated landslide susceptibility, with a continuous SW-NE-trending high-susceptibility strip forming along both banks of the Yangtze River. This spatial pattern is strongly associated with river distribution. Chen et al. [81] identified proximity to rivers as the second most critical factor influencing landslide occurrence. Similarly, Zhou et al. [82] demonstrated the significant impact of river proximity, noting that most landslides occur within 200 m of a river. The nonparametric kernel density analysis in Figure 8 further supports this finding, showing a higher frequency of landslides closer to rivers, particularly within 500 m. Moreover, the region features a dense network of roads, where engineering activities have altered the local geological environment, thereby increasing instability and acting as a significant trigger for landslides. Additionally, as part of the Three Gorges Reservoir Area, periodic fluctuations in reservoir water levels further weaken slope stability, increasing the likelihood of landslides. From the perspective of disaster mechanisms, the geological background, shaped over millions of years or even longer, exhibits relative stability on a large scale. However, the development of surface hydrological systems has eroded riverbank slopes over time, increasing slope instability and creating conditions conducive to disaster. The likelihood of landslides increases significantly under the combined influence of extreme rainfall and other triggering factors.

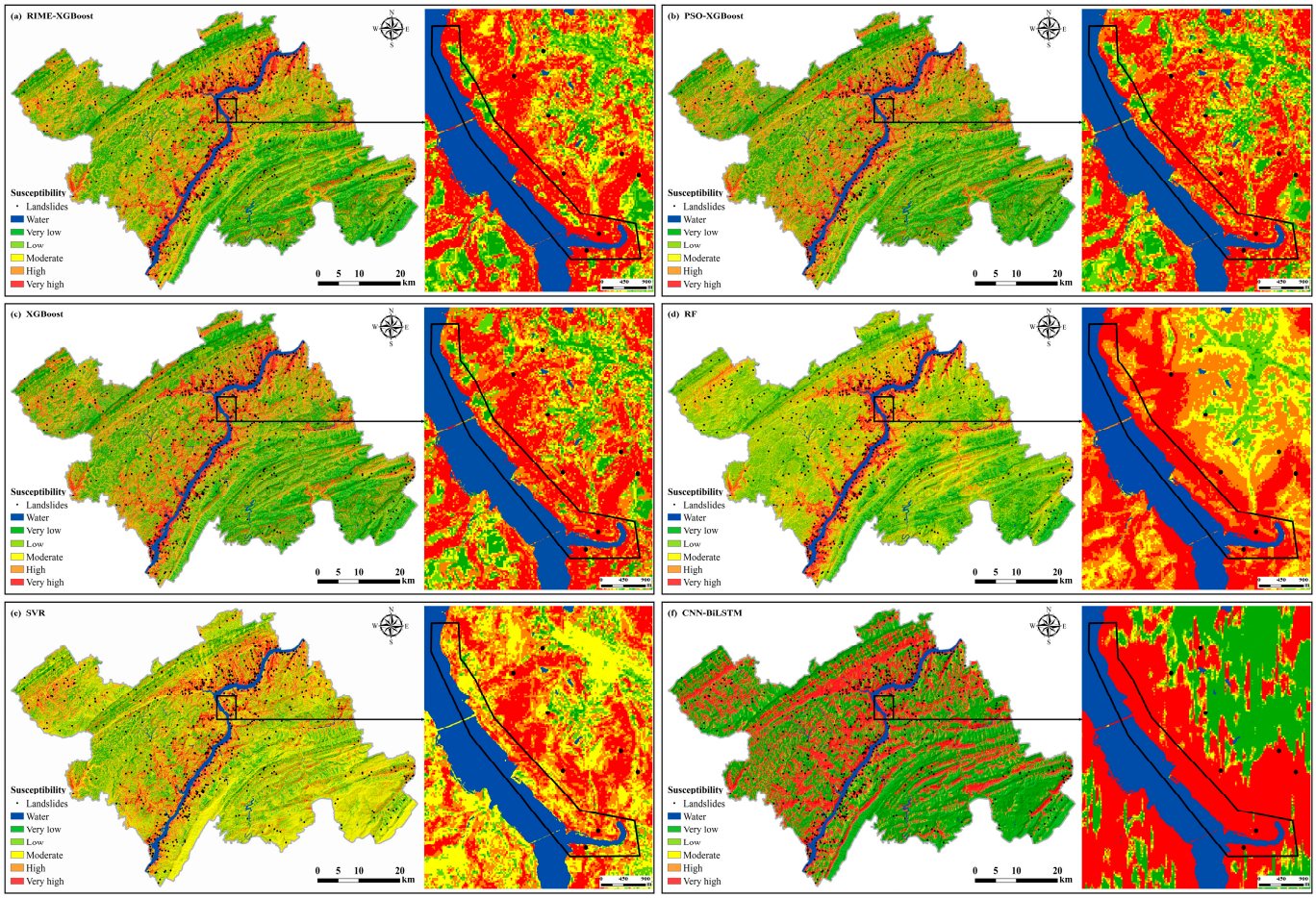


Figure 12. Spatial distributions of the landslide susceptibility for the different models.

Overall, landslide susceptibility is relatively low in the northwest and southeast regions, but the central area of the northwest shows moderate to high susceptibility. According to the landslide susceptibility factors analysis in Figure 2, despite the low elevation and high vegetation cover, the impacts of rivers and roads are still significant. This area is located in Yujia Town, Wanzhou County, where Provincial Road 303 runs southwest–northeast through the town, with a river crossing it and another road along the river. Additionally, farmland and scattered village houses are located along both riverbanks. In the event of a landslide, agricultural land and residential properties would face severe risks. Therefore, this area should be prioritized for monitoring and prevention.

Overall, the LSI spatial distributions generated by all models show high consistency. While the RF model is consistent in general classification, it underperforms in capturing finer details. Balogun et al. [35] successfully used the SVR method for landslide susceptibility mapping in Western Serbia, but in Wanzhou County, the SVR model tended to classify susceptibility as moderate, with limited ability to depict high- and low-susceptibility areas. The CNN-BiLSTM model excels at capturing extreme data points and distinguishing disaster-prone areas, but it falls short in delineating disaster prevention zones, especially in extensive landslide-prone regions like Wanzhou County, where more refined zoning is needed. In contrast, XGBoost and its variants offer a comprehensive view of susceptibility areas and excel in capturing local details. While the LSI spatial distributions generated by the three XGBoost-based models show high similarity, local differences persist. Detailed maps highlight these differences, especially in riverbank areas: regions classified as high susceptibility in the XGBoost and PSO-XGBoost maps are categorized as very high susceptibility in the RIME-XGBoost map. This suggests that RIME-XGBoost provides more

precise details in high-susceptibility areas, reducing redundancy in moderate-susceptibility regions. Despite this, XGBoost demonstrates strong predictive performance, with PSO and RIME further enhancing its accuracy. These results indicate that the landslide susceptibility map generated by the RIME-XGBoost ensemble model is highly practical and reliable.

An analysis of the landslide susceptibility predictions from different models, as shown in Figures 10–12 and Tables 3–5, indicates that the standalone XGBoost model exhibits greater stability in landslide susceptibility prediction compared to other standalone models. Meanwhile, the RIME-XGBoost model proves to be more suitable for the Wanzhou County.

4.2. Landslide Risk Assessment Results

4.2.1. Analysis of Landslide Hazard Assessment Results

The landslide susceptibility results obtained via the RIME-XGBoost model, which demonstrated optimal accuracy, were combined with hazard contributing factors (rainfall erosion intensity and annual average rainfall) to calculate the landslide hazard assessment results for Wanzhou County (Figure 13). The hazard assessment results were categorized into five levels via the natural breaks method: very low, low, moderate, high, and very high.

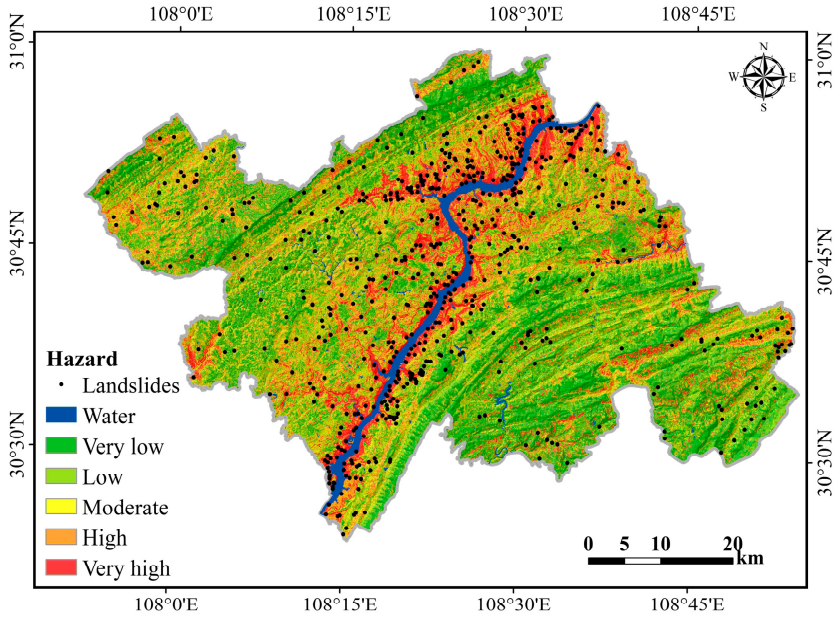


Figure 13. Spatial distribution of the landslide hazard.

The landslide hazard class, area percentage, and landslide percentage are shown in Table A3. The results revealed that the very-high-hazard area contains approximately 77% of the landslides, although it only accounts for approximately 13% of the total area. This finding indicates a relatively concentrated distribution of landslides within the county, which is consistent with the actual situation. In addition, low- and very-low-hazard areas account for more than 50% of the area, which means that in more than half of the county, the impact of natural and human activities is weak, and the probability of landslides is relatively low. Notably, as the hazard level increases from very low to very high, the landslide density also increases, with an increase of approximately 60 times.

Obvious spatial differences were observed in the landslide hazard level of Wanzhou County, with an overall moderately low level. The very-low- and low-hazard zones are distributed mainly in the high-altitude mountainous areas in the north and southeast, whereas the high- and very-high-hazard zones are more concentrated along rivers and central towns. Notably, the overall spatial distribution of landslide hazards is highly consistent

with susceptibility, suggesting that there is a close relationship between the occurrence of geohazards and the geological base environment in which they are located. This finding is highly important for guiding future geohazard prevention and mitigation efforts.

4.2.2. Analysis of Landslide Vulnerability Assessment Result

The area and area percentage for each vulnerability class are specified in Table A4. The areas with very low and low landslide vulnerability levels cover 3051.568 km^2, accounting for approximately 89.712% of the total area. Most areas are sparsely populated and inaccessible. However, highly vulnerable zones, which account for only approximately 3% of the total area, are located mainly in urban regions with high population density, dense buildings and roads, and frequent human activities (Figure 14). Once a landslide occurs, it poses a great threat to people's lives and property.

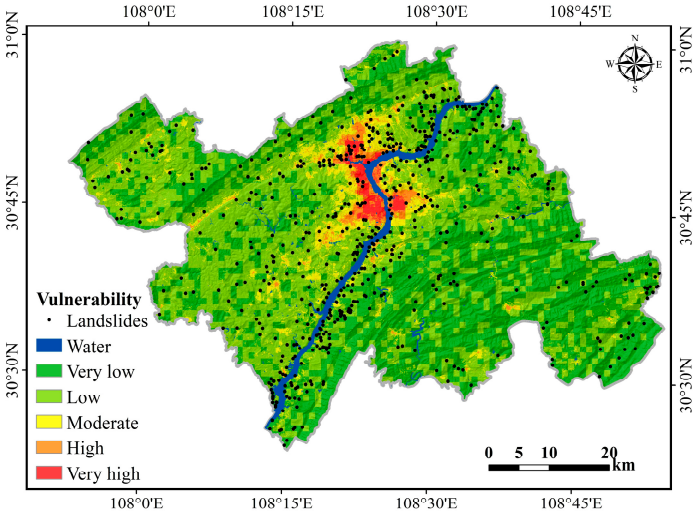


Figure 14. Spatial distribution of landslide vulnerability.

4.2.3. Analysis of Landslide Risk Assessment Result

Combining the landslide hazard and vulnerability, a raster superposition calculation was conducted to obtain the landslide risk in Wanzhou County (Figure 15). Under the combined influence of natural and social factors, the distribution of landslide risk shows certain spatial differentiation characteristics. The vast majority of the area is at a low level of risk, whereas only a few areas are at high or very high risk of landslides.

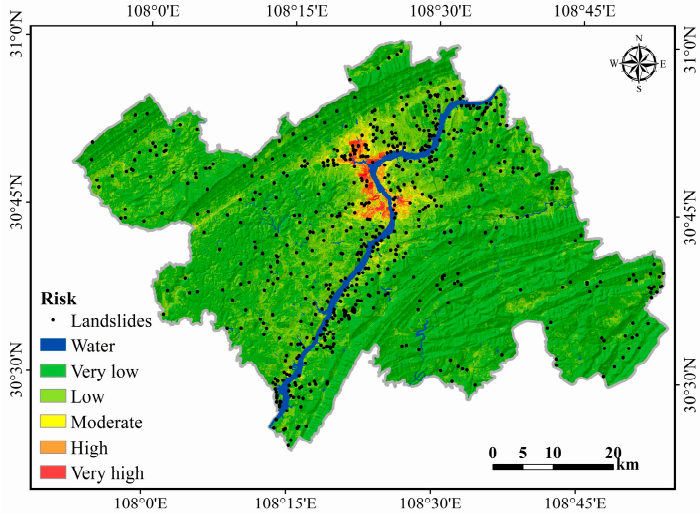


Figure 15. Spatial distribution of the landslide risk.

The very-low-risk area is approximately 2460 km^2, accounting for approximately 72% of the total area, and is located mainly in high-altitude mountainous areas. The low- to moderate-risk areas account for approximately 26% of the total area and are spatially dispersed, mainly in areas along rivers (Table A5). In these areas, farmers exploit geography to cultivate their labor. Therefore, in the event of landslides in these areas, farmers face severe economic and life-destroying damage. Although relatively high-risk areas account for less than 1% of the total area, their geographical location and potential impact cannot be ignored. These areas are mainly concentrated in densely populated urban regions and are highly susceptible to landslides, especially when faced with fluctuating reservoir levels and sudden extreme rainfall. This can cause significant damage and losses. Therefore, we must sufficiently consider these high-risk areas.

4.2.4. Improvement in Landslide Risk Through Enhanced Susceptibility Accuracy: Insights from Multi-Model Comparison

The landslide points shown in Figure 16 were newly identified using high-resolution Google imagery, revealing typical regional landslide characteristics and the effectiveness of the three predictive models. In Figure 16A, areas with vegetation in 2021 show landslides in the 2022 imagery. The region is generally divided into two sides by a southwest–northeast-oriented road, exhibiting a distinct highland–lowland step-like terrain. The western side is elevated, with a maximum altitude exceeding 560 m, while the eastern side is lower, with altitudes ranging from 150 to 220 m. The landslide occurs at the junction of the step-like terrain, with an elevation difference of approximately 30 m. Despite the dense vegetation, the lithology consists of mixed sedimentary rock, a highly susceptible rock type for landslides in Wanzhou County. The slope is approximately 20.6°. Under the combined influence of extreme rainfall and human activities, the area is highly prone to landslide disasters. In the marked region of Figure 16B, the 2019 imagery may be historical landslide remnants (not included in the 709 landslide points of this study), with new landslides appearing in the 2023 imagery. The landslide occurred on the eastern side of a northwest–southeast-oriented main road, which divides the region into lowlands to the west and highlands to the east. The west side has an elevation of approximately 280–310 m, suitable for human activities, with scattered cottages and settlements; the east side is higher, reaching up to 410 m. The landslide took place within an elevation range of 357–370 m, with slopes between 14.7°and 16.5°. The landslide body is adjacent to the road, posing a significant threat. The lithology in this area is also mixed sedimentary rock, further confirming its high susceptibility to landslides in Wanzhou County. The new landslide points, whether in densely or sparsely populated areas, fall within high- or very-high-susceptibility zones predicted by all three models. This confirms that the model predictions align with actual conditions and validate the models' effectiveness in landslide susceptibility prediction, despite minor differences (Tables A6 and A7).

The high-resolution remote sensing image shows landslides reaching the road at the base of the slope, impacting transportation, with numerous residential buildings nearby (Figure 16A). Overlaying the risk maps from the three models with the 2022 imagery shows that the RIME-XGBoost model most accurately represents the risk distribution in populated areas. Although all three models successfully predicted the risk to the buildings in the lower-right corner, XGBoost and PSO-XGBoost underestimated the risk around major roads and nearby buildings, while RIME-XGBoost accurately identified the high-risk areas. This difference is due to the higher accuracy of the RIME-XGBoost model in susceptibility prediction, enabling it to effectively delineate the risk to roads and buildings in landslide-affected zones. Notably, the two rows of parallel houses in the northeast were predicted by RIME-XGBoost to be in moderate- to low-risk zones, while XGBoost and PSO-XGBoost classified them as moderate- to high-risk zones. Based on the regional 3D map analysis,

landslides predominantly occur along a northwest–southeast axis, mainly threatening buildings in the southeastern direction. Located in the northeastern part of the landslide area and at a higher elevation, these two rows of houses face a lesser threat, resulting in a lower risk. Thus, the RIME-XGBoost model demonstrates higher accuracy in predicting risk distribution in densely populated areas, confirming its superiority. Figure 16B shows a sparsely populated area, where all three models predict low risk. The region contains few roads and scattered buildings, with a low population, resulting in a low risk level. The performance of the three models in this area shows little difference.

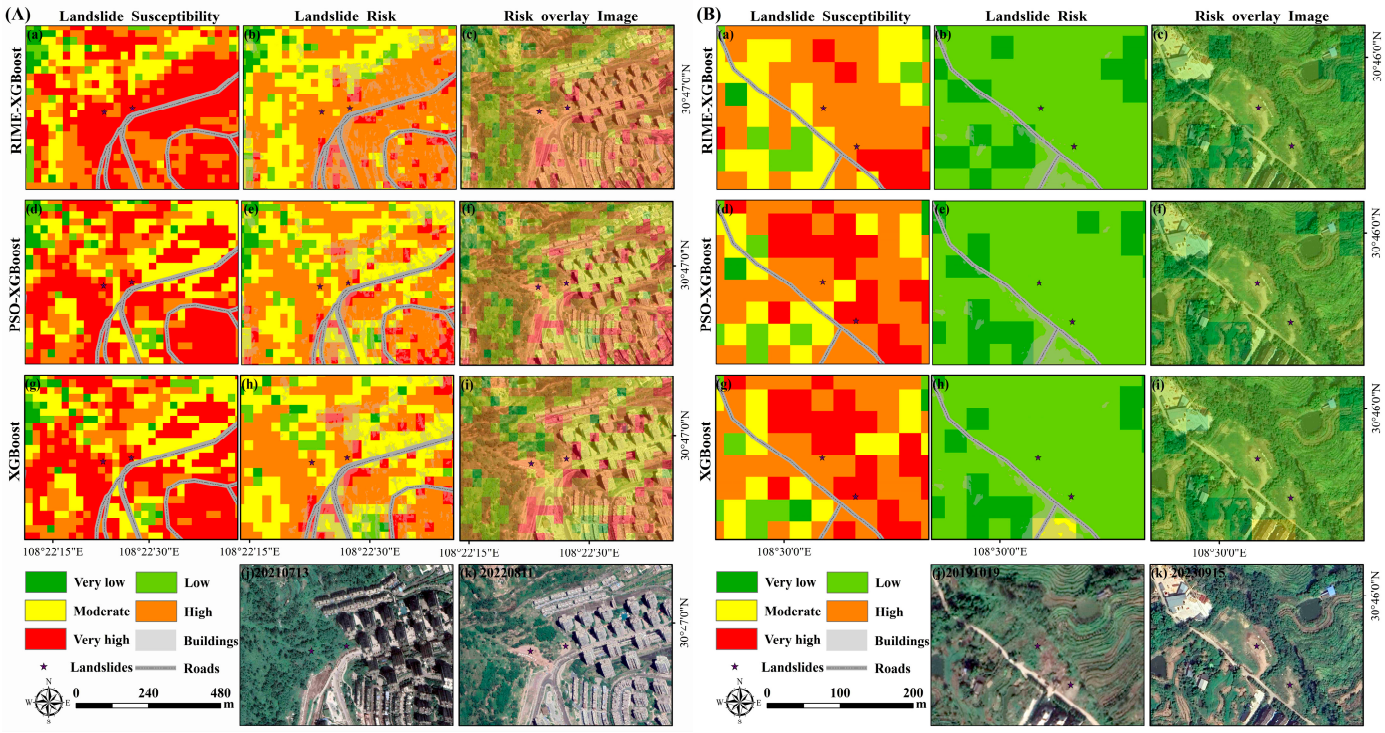


Figure 16. Visualization of the relationship between landslide susceptibility and risk: (**A**) densely populated areas ((Aa), (Ad), and (Ag) show landslide susceptibility, while (Ab), (Ae), and (Ah) show landslide risk, all based on the RIME-XGBoost, PSO-XGBoost, and XGBoost models, respectively. (Ac), (Af), and (Ai) overlay landslide risk with high-resolution imagery (11 August 2022) for the same models. (Aj) and (Ak) show pre-landslide (2021) and post-landslide (2022) images, respectively.) and (**B**) sparsely populated areas ((Ba), (Bd), and (Bg) show landslide susceptibility, while (Bb), (Be), and (Bh) show landslide risk, all based on the RIME-XGBoost, PSO-XGBoost, and XGBoost models, respectively. (Bc), (Bf), and (Bi) overlay landslide risk with high-resolution imagery (15 September 2023) for the same models. (Bj) and (Bk) show pre-landslide (2019) and post-landslide (2023) images).

In summary, the risk assessment results indicate that the RIME-XGBoost model better captures the high-risk spatial distribution in densely populated areas, aligning closely with actual conditions. In sparsely populated areas, the risk predictions from all three models show few differences. Thus, accurate landslide susceptibility predictions enhance the reliability of risk assessments, particularly in populated regions.

5. Discussion

5.1. Landslide Event Validation

Using the landslide events that occurred during the extreme rainfall from 16 to 18 July 2020, in Wanzhou County (with a cumulative rainfall of 202 mm) as an example [83], this study conducts a detailed comparative validation analysis of the actual landslides caused by this rainfall event against the susceptibility and risk assessments obtained in

this research. The results revealed that among the 78 landslides, 60 (77%) were located in areas of moderate to high susceptibility, validating the accuracy of the assessment. A deeper analysis revealed that due to the vast and varied terrain of the study area, along with uneven population and traffic distributions, the landslide risk exhibited a pattern of lower risk in the periphery and higher risk along the urban riverfront. During this rainfall event, 28 landslides (36%) occurred in areas classified as medium- to high-risk, all of which were located within the urban area, demonstrating a high degree of consistency with the risk assessment.

In the region shown in Figure 17a, high susceptibility, proximity to roads, and dense buildings indicate that, in the event of a landslide disaster, the roads act as primary disaster-prone entities, suffering significant economic and human losses, thus highlighting a notable risk. On 16 July 2020, a landslide event (named the Houcaowan landslide) occurred in this area (Group 2, Wanzhou Village, Shahe Street), triggered by heavy rainfall, which directly damaged the outer embankment of the village road. This aligns closely with the map analysis, highlighting the high risk associated with the roads in this area. The landslide was substantial, measuring approximately 30 m wide and 20 to 25 m long, with an average thickness of 1.5 m, resulting in a total volume of nearly 900 cubic meters. Approximately 400 cubic meters of the landslide mass directly impacted National Highway G318 and the surrounding area, exacerbating the damage. The landslide debris consisted of silty clay, sandstone, and 30% gravel. After the event, the rear embankment significantly subsided, leaving the road surface suspended and creating visible cracks in the center, which severely damaged the infrastructure. Moreover, approximately 500 cubic meters of loose debris on the slope of the landslide continues to pose a threat, as it may slide again and jeopardize the safety of National Highway G318, which is located approximately 50 m below. A comparative analysis (Table A8) of the model evaluation results and actual conditions, considering the disaster-causing factors, shows that the lithology of the landslide area is primarily mixed sedimentary rock, with a slope of 18.13°. The area is close to a road and about 340 m from the nearest water system. Long-term river erosion and activities such as road construction have altered the local geological environment, reducing slope stability and increasing landslide susceptibility. Under extreme rainfall conditions, landslides are highly likely. The landslide is adjacent to a road, and downstream, there are clustered buildings and a network of roads (as shown in Google satellite imagery), posing a significant threat to infrastructure. This study's risk assessment results indicate a high risk level for the area, confirming the consistency between the model evaluation and the actual field conditions.

The Xinju landslide (Figure 17b) occurred on 18 July 2020, in the area behind Xinju House in Longbao Village, which is highly susceptible to landslides because of its geographical location. Although the overall risk assessment is at a moderate to high level, the dense buildings in the surrounding area pose a primary safety hazard under the threat of heavy rainfall. Investigative data further confirmed this, as the landslide, after undergoing deformation and destruction, directly impacted a six-story reinforced concrete building at the foot of the slope. This resulted in the rupture of the water supply plastic pipes on the exterior walls, the blockage of drainage ditches, and water accumulation, which severely threatened the lives and property safety of 37 people living in 12 households within the building. A comparative analysis of the model evaluation results and actual field conditions, considering the disaster-causing factors, indicates that the landslide area is approximately 134 m from the road and about 424 m from the nearest water system. The landslide occurred on a slope of 17.9°. Google satellite imagery reveals that the surrounding area consists of extensive agricultural land and buildings, all of which are under significant threat. The risk assessment results show that the landslide is situated in a high-risk area,

consistent with the actual field conditions. These findings further validate the assessment of landslide risk and its potential impacts in the region.

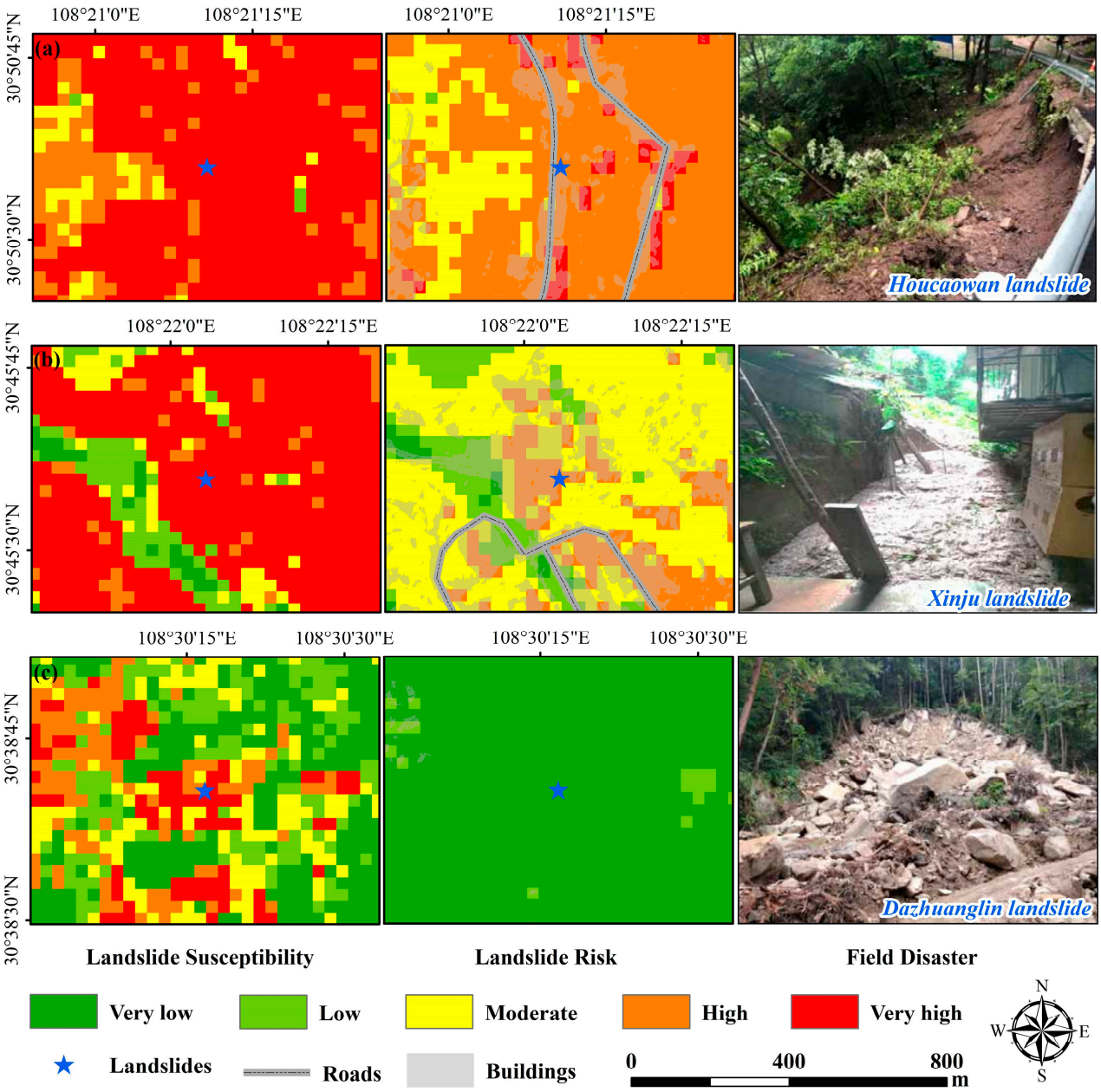


Figure 17. Landslide events ((**a**–**c**) represent the Houcouwan, Xinju, and Dazhuanglin landslides, respectively, showing landslide susceptibility, risk, and a real-world image from left to right) (field disaster images were modified from [83]).

The Dazhuanglin landslide (Figure 17c) occurred on 16 July 2020, in Group 1 of Zhaomu Village, Cizhu Township. The landslide was substantial, measuring approximately 20 m in width and 15 m in length, with an average thickness of 3 m, totaling an estimated volume of 900 cubic meters. It was composed of gray-yellow sandstone gravel, cohesive soil, and sand. Data confirmed that heavy rainfall was the direct trigger of the landslide. Fortunately, there were no casualties or property damage. An analysis of multi-source geological and geographic data indicates that the region's annual precipitation is approximately 1862 mm, significantly higher than that of surrounding areas, with an elevation of about 810 m. The landslide occurred on a steep slope with a gradient of

21.87°, less than 1 km from the main fault and approximately 2 km from the nearest water system. The combined effect of these disaster-causing factors results in higher susceptibility in this area compared to the surrounding regions. Although the area is classified as a high-landslide-susceptibility zone, the landslide's location, distant from urban areas, with limited transportation access and few surrounding buildings and inhabitants, results in a relatively low direct threat to the population, economy, and transportation infrastructure, leading to an overall lower risk. Given the potential for strong rainfall to trigger additional landslides, relevant departments should enhance monitoring and early warning systems to ensure regional safety.

5.2. Improved Landslide Susceptibility Model for Enhanced Spatial Risk Assessment Reliability

To improve the accuracy of risk assessment, this study focuses on constructing a more precise and detailed spatial distribution model of landslide susceptibility. The RIME-XGBoost model accurately predicts high-susceptibility zones, particularly roads and buildings in densely populated areas, by effectively capturing the relationship between landslide events and influencing factors, leading to more reliable risk forecasts. This study, using regional three-dimensional maps, further validates the superiority of the RIME-XGBoost model. Specifically, in predicting the risk of two parallel rows of houses in the northeastern region (Figure 16A), the model accurately identified the lower risk based on factors like elevation and aspect, while XGBoost and PSO-XGBoost misclassified it as higher risk. This highlights the model's improved accuracy in correctly identifying susceptible areas and preventing misjudgments, offering more precise data for disaster prevention.

However, the current understanding remains insufficient. In the future, once more accurate data become available—such as the intensity of landslide bodies, the population's perception, and response capabilities regarding landslide risks, as well as data on casualties and economic losses caused by landslides—the landslide risk results will be updated with greater precision and timeliness, enabling a better understanding of the patterns and mechanisms of the spatial distribution of landslide risks.

5.3. Integrated Landslide Risk Assessment Results to Guide Prevention and Control Strategies

This study conducted a comprehensive assessment of landslide risk in Wanzhou County, revealing that the central urban area and its surrounding regions face a high level of risk. This high-risk situation primarily arises from two factors: first, the high-intensity human activities within the central urban area, including the dense construction of high-rise buildings, the expansion of transportation networks, and large-scale alterations to the geological environment (such as slope excavation), significantly reduce the stability of natural slopes and promote the occurrence of landslides; second, the unique geographical location of Wanzhou County, where towns are distributed along both banks of the Yangtze River, combined with the periodic fluctuations in reservoir water levels caused by the Three Gorges Reservoir, collectively exacerbates the landslide risk along the Yangtze River.

Given the vastness of the study area, this assessment initially focused on rain-related factors for landslide hazard analysis. While this represents an important step toward understanding regional landslide risk, there remains room for improvement in terms of accuracy and comprehensiveness. To further optimize the assessment model, future research should carefully consider changes in reservoir water levels as critical triggering factors and comprehensively evaluate the mitigation effects of disaster prevention and reduction engineering measures on landslide risk, aiming to establish a more precise and comprehensive risk assessment system. Nevertheless, the risk zoning results of this study provide an important reference for relevant authorities and contribute to the development of more effective risk prevention and control strategies.

In high-risk urban areas characterized by high population density and economic development, detailed disaster prevention strategies must be implemented. Given that the region is prone to rain-induced landslides, it is essential to strengthen the meteorological monitoring and early warning system, integrating high-tech methods to achieve high-precision, round-the-clock monitoring. In addition, the following measures should be considered: establishing a predisaster warning and emergency response linkage mechanism to ensure efficient information dissemination; increasing the number of shelters to increase public evacuation capabilities and reduce casualties; and implementing slope stabilization measures and optimizing groundwater management to lower landslide risk. For low-risk areas, regular risk assessments should be conducted, and disaster prevention education should be strengthened to enhance societal disaster preparedness. In the long term, promoting ecological restoration is necessary to increase the stability of ecosystems, fundamentally reduce disaster risk, and foster the harmonious coexistence and sustainable development of the regional economy, society, and environment.

5.4. Prospects for a Comprehensive Risk Evaluation Framework for Landslides from a Multi-Model Perspective

This study successfully optimized the XGBoost model by finely adjusting its hyperparameters and systematically compared the optimized model with the unoptimized version. The results indicate that the optimized XGBoost model significantly improves the accuracy of landslide susceptibility prediction (as shown in Section 4.1.3), which in turn enhances the overall performance of landslide risk prediction (as discussed in Section 5.1). However, importantly, the current research focuses on the effects of optimizing the internal parameters of a single model (XGBoost) and does not consider the coupling between the model and underlying patterns. In the future, multi-model integration will be the core strategy of the landslide risk assessment framework. This means that this strategy will no longer be limited to a single model or method but rather a combination of multiple models and methods with complementary properties that together support the comprehensive assessment of landslide risk. These models may include material models, statistical models, machine learning models, etc., that can reveal the causes and mechanisms of landslide risk from different perspectives and at different levels. In terms of model integration and coordination, future studies need to give attention to the differences and conflicts between different models and achieve consistency and reliability of the evaluation results with the help of optimization algorithms and technical means such as decision support systems to ensure the validity and stability of multi-model comprehensive evaluation frameworks. In addition, the interpretation and visualization of the results are key aspects of future development, enabling the evaluation results to be communicated to decision-makers, stakeholders, and the public through easy-to-understand diagrams and reports to improve the knowledge and understanding of landslide risks and enhance the ability to prevent and respond to disasters.

6. Conclusions

This study proposes a hybrid model combining XGBoost and the RIME optimization algorithm. RIME can effectively select features and assign weights by simulating the process of rime frost ice formation, overcoming the overfitting issue of XGBoost in handling high-dimensional features, reducing complexity, and improving prediction accuracy. Additionally, the influencing factors of landslide disasters in Wanzhou County were analyzed in depth. By integrating landslide susceptibility, dynamic factors, and social vulnerability, a comprehensive landslide risk index was developed. A spatial distribution map of the integrated landslide risk in Wanzhou County was then generated, identifying

regions with varying levels of landslide risk due to the spatial heterogeneity of geological, environmental, and socio-economic factors. The conclusions are as follows:

(1) The RIME-XGBoost-based landslide susceptibility model shows the smallest expectation and super-entropy, indicating the accuracy and stability of the RIME-XGBoost predictions. Additionally, the XGBoost model optimized by RIME outperforms the standard XGBoost model, with an AUC score of 0.947 and an increase of 0.064. Compared to other models, its accuracy improved by up to 0.15.

(2) Landslide susceptibility results show that landslides are mainly concentrated in high- and very-high-susceptibility zones. While the very-high-susceptibility zone covers only 8% of the area, it includes 82% of the landslides. A high-susceptibility corridor runs southwest–northeast along the Yangtze River, likely due to complex geology and river erosion. A risk assessment indicates that 72% of the region has a very low landslide risk, with 26% having a low to moderate risk. High- and very-high-risk areas, covering just over 1% of the total area, are concentrated in urban centers, where dense populations, economic activity, and infrastructure elevate the risk.

(3) This study examines how landslide susceptibility predictions influence landslide risk modeling. In high-risk areas with dense populations, the RIME-XGBoost model accurately predicted risks to buildings and roads, aligning with actual conditions, while XGBoost and PSO-XGBoost both underestimated the risk. In sparsely populated areas, the risk predictions from all three XGBoost-based models showed minimal differences. Thus, RIME-XGBoost offers a more precise depiction of high-risk zones in populated regions, enhancing the reliability of risk assessment.

This study proposes a reliable and comprehensive landslide risk assessment framework for decision-makers, applicable to regions with similar geological conditions, particularly mountainous areas characterized by high rainfall. The framework not only provides a scientific foundation for spatial planning but also offers critical insights for enhancing urban safety and safeguarding the ecological environment.

Author Contributions: Conceptualization, X.D. and J.C.; methodology, X.D.; software, X.D. and T.Z.; validation, C.X.; formal analysis, X.D.; investigation, X.D. and J.C.; resources, J.C.; data curation, X.D. and T.Z.; writing—original draft preparation, X.D.; writing—review and editing, J.C. and T.Z.; visualization, X.D. and T.Z.; supervision, J.C. and C.X.; project administration, J.C.; funding acquisition, J.C. All authors have read and agreed to the published version of the manuscript.

Funding: This research was funded by the National Key Research and Development Program of China, grant number 2023YFC2906404, and the Geological Survey Projects of the China Geological Survey, grant number DD20230408.

Data Availability Statement: The data presented in this study are available upon request from the corresponding author.

Acknowledgments: The authors would like to thank the anonymous reviewers for their valuable feedback.

Conflicts of Interest: The authors declare no conflicts of interest.

Appendix A

Table A1. Landslide events in Wanzhou County.

Date	Location	Volume (m^3)	Description	Source
29 July 2024	Group 4, Yanzi Village, Xiong Family Town	1200	House damage	https://www.cqrb.cn/jingji/zixun/2024-07-30/1981598_pc.html (accessed on 15 August 2024)
17 July 2024	Group 3, Maidiping, Fuqiang Village, Tiefeng Township	----	Cracks formed at the landslide edge, posing safety risks	https://new.qq.com/rain/a/20240722A04ISH00 (accessed on 15 August 2024)
4 July 2023	Shatan village, Changtan township	----	House collapse, three people buried after heavy rainstorm	https://new.qq.com/rain/a/20230706A01WE400 (accessed on 15 January 2024)
30 June 2023	Banshui town	----	Buried a residential house, killing six people	https://new.qq.com/rain/a/20230701A0685O00 (accessed on 15 January 2024)
26 August 2021	Yujia Town-Kaijiang County Road	----	Caused road disruption and river blockage	https://wanzhou.cbg.cn/show/6619-152911.html (accessed on 15 January 2024)
23 August 2021	Yunyang-Longju section, Provincial Highway 507	2000	Caused road disruption	
16 July 2020	Intersection of National Highway 318 and Longli Village	Over 4000	Temporary interruption of National Highway 318	https://tv.cctv.com/2020/07/24/VIDEym0XcEPdSXaYK8uztHQJ200724.shtml?spm=C53156045404.P4HrRJ64VBfu.0.0 (accessed on 15 January 2024)
16 July 2020	Intersection of National Highway 318 and Road to Xiangtan Community Group 3	Over 20,000	Road damage	
4 April 2013	Sunjia township	1.5 million	Horizontal movement of 30 m; destroyed roads, terraces, and houses	[84,85]

Table A2. Statistical results for the different classes of landslide susceptibility for the different models.

Model	Proportion	Landslide Susceptibility Class				
		Very Low	Low	Moderate	High	Very High
XGBoost	Landslide proportion (%)	2.539	3.808	2.821	5.219	85.614
	Area proportion (%)	32.691	21.162	15.394	16.759	13.993
PSO-XGBoost	Landslide proportion (%)	2.962	3.385	3.808	5.078	84.767
	Area proportion (%)	35.793	20.447	16.675	15.730	11.356
RIME-XGBoost	Landslide proportion (%)	2.821	3.808	6.065	4.937	82.370
	Area proportion (%)	33.433	22.786	20.800	14.684	8.297

Table A3. Statistical results for different classes of landslide hazard.

Class	Very Low	Low	Moderate	High	Very High
Landslide proportion (%)	2.821	4.654	7.898	7.898	76.728
Area proportion (%)	28.865	22.350	20.157	15.507	13.121

Table A4. Statistical results for the different classes of landslide vulnerability.

Class	Very Low	Low	Moderate	High	Very High
Area (km^2)	1467.765	1583.803	241.571	69.797	38.59
Area proportion (%)	43.15	46.562	7.102	2.052	1.134

Table A5. Statistical results for the different classes of landslide risk.

Class	Very Low	Low	Moderate	High	Very High
Area (km^2)	2458.325	825.300	74.617	29.603	13.297
Area proportion (%)	72.279	24.265	2.194	0.870	0.391

Table A6. Spatial distribution characteristics of landslide susceptibility and risk under different models considering actual disaster influence factors in densely populated areas.

Model	Spatial Distribution Characteristics of Susceptibility		Spatial Distribution Characteristics of Risk		Analysis of Disaster-Causing Factors
	Similarities	Differences	Similarities	Differences	
RIME-XGBoost	The spatial distribution of susceptibility within the region is distinct, with the area in the lower-right corner exhibiting a high level of susceptibility.	Within the region, areas along the main road (generally oriented southwest–northeast) and its surrounding zones exhibit very high susceptibility.	The spatial distribution of risk within the region is distinct, with the area in the lower-right corner exhibiting a high level of risk.	The areas along the main road and the nearby buildings are classified as high-risk.	The region is divided by a southwest–northeast road, creating a distinct highland–lowland terrain. The western side exceeds 560 m in altitude, while the eastern side ranges from 150 to 220 m. The landslide occurs at the junction of these terrains, with an elevation difference of about 30 m. Despite dense vegetation, the mixed sedimentary rock lithology, a highly susceptible type in Wanzhou County, combined with a 20.6° slope, makes the area prone to landslides, especially under extreme rainfall and human influence.
PSO-XGBoost		Around the main road segments, approximately half of the area exhibits moderate susceptibility.		Approximately half of the areas along the main road are classified as moderate-risk. The risk in some road and building areas has been underestimated.	
Model					

Table A7. Spatial distribution characteristics of landslide susceptibility and risk under different models considering actual disaster influence factors in sparsely populated areas.

Model	Spatial Distribution Characteristics of Susceptibility		Spatial Distribution Characteristics of Risk	Analysis of Disaster-Causing Factors
	Similarities	Differences		
RIME-XGBoost	The spatial distribution of susceptibility within the region is distinct, with an overall high level of susceptibility.	The susceptibility on the east side of the road is predominantly high, while the west side is primarily moderate.	All three models show a low overall risk level for the region, despite minimal differences.	The landslide occurred at 357–370 m elevation, with slopes of 14.7–16.5°. The landslide body, adjacent to the road, poses a significant threat. The area's mixed sedimentary rock lithology further confirms its high landslide susceptibility in Wanzhou County.
PSO-XGBoost		The susceptibility on the east side of the road ranges from high to very high, while the west side is primarily moderate to high.		
Model				

Table A8. Comparison of model evaluation results with actual conditions considering disaster influence factors.

Landslide Name	Time	Landslide Overview and Causes	Field Disaster Images	Comparison of Model Evaluation Results and Actual Conditions Incorporating Disaster-Causing Factors
Houcaowan landslide	16 July 2020	The landslide, 30 m wide, 20 to 25 m long, and 1.5 m thick, with a volume of 900 m^3, impacted National Highway G318. Composed of silty clay, sandstone, and 30% gravel, the debris caused embankment subsidence, suspending the road and creating cracks. Around 500 cubic meters of loose debris remain, threatening the highway, 50 m below. Heavy rainfall directly triggered the landslide.		The landslide area, with mixed sedimentary rocks and an 18.13° slope, is near a road and 340 m from the nearest water system. River erosion and road construction have weakened slope stability, increasing landslide risk. Extreme rainfall heightens the likelihood of landslides. The area, with nearby roads and buildings, poses a significant infrastructure threat. The risk assessment confirms a high risk level, consistent with field conditions.
Xinju landslide	18 July 2020	The landslide was located behind the new houses of Longbao Village, with a width of approximately 30 m, a length of about 15 m, an average thickness of 15 m, and a volume of approximately 500 cubic meters. The landslide's mass was primarily composed of silty clay, with about 10% gravel content. After deformation, the landslide locally collapsed by approximately 10 m, directly impacting the new houses at the base of the steep slope. Heavy rainfall was the direct trigger of the landslide.		The landslide area is approximately 134 m from the road and about 424 m from the nearest water system. It occurred on a slope of 17.9°. Google satellite imagery shows that the surrounding area consists of extensive agricultural land and buildings, all of which are under significant threat. The risk assessment results indicate that the landslide is located in a high-risk area, consistent with the actual field conditions.
Dazhuanglin landslide	16 July 2020	The landslide occurred in Group 1 of Zhaomu Village, Cizhu Township. It was substantial, measuring approximately 20 m in width and 15 m in length, with an average thickness of 3 m and an estimated volume of 900 cubic meters. The landslide consisted of gray-yellow sandstone gravel, cohesive soil, and sand. Data confirmed that heavy rainfall was the direct trigger. Fortunately, there were no casualties or property damage.		With 1862 mm of annual rainfall and an elevation of 810 m, the region is more prone to landslides. The event occurred on a 21.87° slope, near the main fault and 2 km from the water system. While classified as high susceptibility, the remote location, limited access, and few nearby buildings reduce the risk to the people, economy, and infrastructure.

References

1. Wang, X.; Wang, Y.; Lin, Q.; Yang, X. Assessing Global Landslide Casualty Risk Under Moderate Climate Change Based on Multiple GCM Projections. *Int. J. Disaster Risk Sci.* **2023**, *14*, 751–767. [CrossRef]
2. Sim, K.B.; Lee, M.L.; Wong, S.Y. A review of landslide acceptable risk and tolerable risk. *Geoenviron. Disasters* **2022**, *9*, 3. [CrossRef]
3. Fidan, S.; Tanyaş, H.; Akbaş, A.; Lombardo, L.; Petley, D.N.; Görüm, T. Understanding fatal landslides at global scales: A summary of topographic, climatic, and anthropogenic perspectives. *Nat. Hazards* **2024**, *120*, 6437–6455. [CrossRef]
4. Dai, F.C.; Lee, C.F.; Ngai, Y.Y. Landslide risk assessment and management: An overview. *Eng. Geol.* **2002**, *64*, 65–87. [CrossRef]
5. Huang, Y.; Zhao, L. Review on landslide susceptibility mapping using support vector machines. *Catena* **2018**, *165*, 520–529. [CrossRef]
6. Tian, N.; Lan, H. The indispensable role of resilience in rational landslide risk management for social sustainability. *Geogr. Sustain.* **2023**, *4*, 70–83. [CrossRef]
7. Flentje, P.; Chowdhury, R. Resilience and sustainability in the management of landslides. *Proc. Inst. Civ. Eng.-Eng. Sustain.* **2018**, *171*, 3–14. [CrossRef]
8. Perera, E.N.C.; Jayawardana, D.T.; Jayasinghe, P.; Bandara, R.M.S.; Alahakoon, N. Direct impacts of landslides on socio-economic systems: A case study from Aranayake, Sri Lanka. *Geoenviron. Disasters* **2018**, *5*, 11. [CrossRef]
9. Lacroix, P.; Handwerger, A.L.; Bièvre, G. Life and death of slow-moving landslides. *Nat. Rev. Earth Environ.* **2020**, *1*, 404–419. [CrossRef]
10. IFRC. *2020 Global Natural Disaster Assessment Report*; IFRC: Geneva, Switzerland, 2021.
11. UNOCHA. *Asia and the Pacific: Weekly Regional Humanitarian Snapshot (6–13 August 2019)*; UNOCHA: New York, NY, USA, 2019.
12. Froude, M.J.; Petley, D.N. Global fatal landslide occurrence from 2004 to 2016. *Nat. Hazards Earth Syst. Sci.* **2018**, *18*, 2161–2181. [CrossRef]
13. Chen, W.; Xie, X.; Wang, J.; Pradhan, B.; Hong, H.; Bui, D.T.; Duan, Z.; Ma, J. A comparative study of logistic model tree, random forest, and classification and regression tree models for spatial prediction of landslide susceptibility. *Catena* **2017**, *151*, 147–160. [CrossRef]
14. Jemec Auflič, M.; Bezak, N.; Šegina, E.; Frantar, P.; Gariano, S.L.; Medved, A.; Peternel, T. Climate change increases the number of landslides at the juncture of the Alpine, Pannonian and Mediterranean regions. *Sci. Rep.* **2023**, *13*, 23085. [CrossRef] [PubMed]
15. Liu, J.; Wu, Y.; Gao, X. Increase in occurrence of large glacier-related landslides in the high mountains of Asia. *Sci. Rep.* **2021**, *11*, 1635. [CrossRef] [PubMed]
16. Alcántara-Ayala, I.; Sassa, K. Landslide risk management: From hazard to disaster risk reduction. *Landslides* **2023**, *20*, 2031–2037. [CrossRef]
17. Yong, C.; Dong, J.; Fei, G.; Bin, T.; Tao, Z.; Hao, F.; Li, W.; Qinghua, Z. Review of landslide susceptibility assessment based on knowledge mapping. *Stoch. Environ. Res. Risk Assess.* **2022**, *36*, 2399–2417. [CrossRef]
18. Sezer, E.A.; Nefeslioglu, H.A.; Osna, T. An expert-based landslide susceptibility mapping (LSM) module developed for Netcad Architect Software. *Comput. Geosci.* **2017**, *98*, 26–37. [CrossRef]
19. Lyu, H.-M.; Shen, J.S.; Arulrajah, A. Assessment of Geohazards and Preventative Countermeasures Using AHP Incorporated with GIS in Lanzhou, China. *Sustainability* **2018**, *10*, 304. [CrossRef]
20. Shahabi, H.; Hashim, M.; Ahmad, B.B. Remote sensing and GIS-based landslide susceptibility mapping using frequency ratio, logistic regression, and fuzzy logic methods at the central Zab basin, Iran. *Environ. Earth Sci.* **2015**, *73*, 8647–8668. [CrossRef]
21. Hu, Q.; Zhou, Y.; Wang, S.; Wang, F. Machine learning and fractal theory models for landslide susceptibility mapping: Case study from the Jinsha River Basin. *Geomorphology* **2020**, *351*, 106975. [CrossRef]
22. Xiong, J.; Zhu, J.; Su, P.; Gong, Y.; Zhao, Y.; Li, J.; Li, W. Risk Assessment of Landslide in the Xiluodu Reservoir Area Based on GIS and Information Value Method. *Resour. Environ. Yangtze Basin* **2019**, *28*, 700–711.
23. Zhang, Y.-X.; Lan, H.-X.; Li, L.-P.; Wu, Y.-M.; Chen, J.-H.; Tian, N.-M. Optimizing the frequency ratio method for landslide susceptibility assessment: A case study of the Caiyuan Basin in the southeast mountainous area of China. *J. Mt. Sci.* **2020**, *17*, 340–357. [CrossRef]
24. Liu, L.; Gao, H. Landslide susceptibility assessment using the coupling of WOE and logistic regression models. *J. Eng. Geol.* **2023**, *31*, 165–175.
25. Zhang, Z.; Deng, M.; Xu, S.; Zhang, Y.; Fu, H.; Li, Z. Comparison of landslide susceptibility assessment models in Zhenkang County, Yunnan Province, China. *Chin. J. Rock Mech. Eng.* **2022**, *41*, 157–171.
26. Wu, R.; Hu, X.; Mei, H.; He, J.; Yang, J. Spatial susceptibility assessment of landslides based on random forest: A case study from Hubei section in the Three Gorges Reservoir area. *Earth Sci.* **2021**, *46*, 321–330.
27. Liu, J.; Liang, E.; Xu, S.; Liu, M.; Wang, Y.; Zhang, F.; Luo, A. Multi-kernel support vector machine considering sample optimization selection for analysis and evaluation of landslide disaster susceptibility. *Acta Geod. Cartogr. Sin.* **2022**, *51*, 2034–2045.
28. Huang, W.; Ding, M.; Wang, D.; Jiang, L.; Li, Z. Evaluation of landslide susceptibility based on layer adaptive weighted convolutional neural network model along Sichuan-Tibet traffic corridor. *Earth Sci.* **2022**, *47*, 2015–2030.

29. Huang, F.; Cao, Z.; Guo, J.; Jiang, S.-H.; Li, S.; Guo, Z. Comparisons of heuristic, general statistical and machine learning models for landslide susceptibility prediction and mapping. *Catena* **2020**, *191*, 104580. [CrossRef]
30. Jiang, Z.; Wang, M.; Liu, K. Comparisons of Convolutional Neural Network and Other Machine Learning Methods in Landslide Susceptibility Assessment: A Case Study in Pingwu. *Remote Sens.* **2023**, *15*, 798. [CrossRef]
31. Huang, W.; Ding, M.; Li, Z.; Yu, J.; Ge, D.; Liu, Q.; Yang, J. Landslide susceptibility mapping and dynamic response along the Sichuan-Tibet transportation corridor using deep learning algorithms. *Catena* **2023**, *222*, 106866. [CrossRef]
32. Janizadeh, S.; Bateni, S.M.; Jun, C.; Pal, S.C.; Band, S.S.; Chowdhuri, I.; Saha, A.; Tiefenbacher, J.P.; Mosavi, A. Potential impacts of future climate on the spatio-temporal variability of landslide susceptibility in Iran using machine learning algorithms and CMIP6 climate-change scenarios. *Gondwana Res.* **2023**, *124*, 1–17. [CrossRef]
33. Shua, Q.; Peng, H.; Li, J. Landslide susceptibility prediction modelling based on semi-supervised XGBoost model. *Geol. J.* **2024**, *59*, 2655–2667. [CrossRef]
34. Zhang, W.; He, Y.; Wang, L.; Liu, S.; Meng, X. Landslide susceptibility mapping using random forest and extreme gradient boosting: A case study of Fengjie, Chongqing. *Geol. J.* **2023**, *58*, 2372–2387. [CrossRef]
35. Balogun, A.-L.; Rezaie, F.; Quoc Bao, P.; Gigovic, L.; Drobnjak, S.; Aina, Y.A.; Panahi, M.; Yekeen, S.T.; Lee, S. Spatial prediction of landslide susceptibility in western Serbia using hybrid support vector regression (SVR) with GWO, BAT and COA algorithms. *Geosci. Front.* **2021**, *12*, 101104. [CrossRef]
36. Reichenbach, P.; Rossi, M.; Malamud, B.D.; Mihir, M.; Guzzetti, F. A review of statistically-based landslide susceptibility models. *Earth Sci. Rev.* **2018**, *180*, 60–91. [CrossRef]
37. Wang, Q.; Xiong, J.; Cheng, W.; Cui, X.; Pang, Q.; Liu, J.; Chen, W.; Tang, H.; Song, N. Landslide susceptibility mapping methods coupling with statistical methods, machine learning models and clustering algorithms. *J. Geo-Inf. Sci.* **2024**, *26*, 620–637.
38. Sun, D.; Xu, J.; Wen, H.; Wang, D. Assessment of landslide susceptibility mapping based on Bayesian hyperparameter optimization: A comparison between logistic regression and random forest. *Eng. Geol.* **2021**, *281*, 105972. [CrossRef]
39. Le Thi, L.; Hoang, N.; Zhou, J.; Dou, J.; Moayedi, H. Estimating the heating load of buildings for smart city planning using a novel artificial intelligence technique PSO-XGBoost. *Appl. Sci.* **2019**, *9*, 2714. [CrossRef]
40. Ding, C.; Wang, X.; Chen, T.; Yu, T. Application of Bayesian optimized XGBoost in seismic interpretation of small-scale faults. *J. China Coal Soc.* **2023**, *48*, 2530–2539.
41. Su, H.; Zhao, D.; Heidari, A.A.; Liu, L.; Zhang, X.; Mafarja, M.; Chen, H. RIME: A physics-based optimization. *Neurocomputing* **2023**, *532*, 183–214. [CrossRef]
42. Sultana, N.; Tan, S.; Hossen, M.F. Landslide risk assessment by integrating hazards and vulnerability indices in Southeast Bangladesh. *Int. J. Disaster Risk Reduct.* **2024**, *114*, 104991. [CrossRef]
43. Chang, M.; Dou, X.; Zhu, X.; Ma, Y. Integrated risk assessment of landslide in karst terrains: Advancing landslides management in Beiliu City, China. *Int. J. Appl. Earth Obs. Geoinf.* **2024**, *132*, 104046. [CrossRef]
44. Liu, X.; Miao, C. Large-scale assessment of landslide hazard, vulnerability and risk in China. *Geomat. Nat. Hazards Risk.* **2018**, *9*, 1037–1052. [CrossRef]
45. Ferrer, J.; Guo, Z.; Medina, V.; Puig-Polo, C.; Hurlimann, M. A framework to project future rainfall scenarios: An application to shallow landslide-triggering summer rainfall in Wanzhou County, China. *Water* **2022**, *14*, 873. [CrossRef]
46. Zhang, S.; Bai, L.; Li, Y.; Li, W.-L.; Xie, M. Comparing Convolutional Neural Network and Machine Learning Models in Landslide Susceptibility Mapping: A Case Study in Wenchuan County. *Front. Environ. Sci.* **2022**, *10*, 886841. [CrossRef]
47. Xu, Y.; Ouyang, C.; Xu, Q.; Wang, D.; Zhao, B.; Luo, Y. CAS Landslide Dataset: A Large-Scale and Multisensor Dataset for Deep Learning-Based Landslide Detection. *Sci. Data* **2024**, *11*, 12. [CrossRef]
48. Pokharel, B.; Alvioli, M.; Lim, S. Assessment of earthquake-induced landslide inventories and susceptibility maps using slope unit-based logistic regression and geospatial statistics. *Sci. Rep.* **2021**, *11*, 21333. [CrossRef]
49. Bhuyan, K.; Tanyaş, H.; Nava, L.; Puliero, S.; Meena, S.R.; Floris, M.; van Westen, C.; Catani, F. Generating multi-temporal landslide inventories through a general deep transfer learning strategy using HR EO data. *Sci. Rep.* **2023**, *13*, 162. [CrossRef]
50. Zhao, Z.; Xu, Z.; Hu, C.; Wang, K.; Ding, X. Geographically weighted neural network considering spatial heterogeneity for landslide susceptibility mapping: A case study of Yichang City, China. *Catena* **2024**, *234*, 107590. [CrossRef]
51. Zhang, J.; Ma, X.; Zhang, J.; Sun, D.; Zhou, X.; Mi, C.; Wen, H. Insights into geospatial heterogeneity of landslide susceptibility based on the SHAP-XGBoost model. *J. Environ. Manag.* **2023**, *332*, 117357. [CrossRef]
52. Lee, S. Current and future status of GIS-based landslide susceptibility mapping: A literature review. *Korean J. Remote Sens.* **2019**, *35*, 179–193. [CrossRef]
53. Rabby, Y.W.; Ishtiaque, A.; Rahman, M.S. Evaluating the effects of digital elevation models in landslide susceptibility mapping in Rangamati District, Bangladesh. *Remote Sens.* **2020**, *12*, 2718. [CrossRef]
54. Yu, L.; Wang, Y.; Pradhan, B. Enhancing landslide susceptibility mapping incorporating landslide typology via stacking ensemble machine learning in Three Gorges Reservoir, China. *Geosci. Front.* **2024**, *15*, 101802. [CrossRef]

55. Zhang, Z.; Sun, J. Regional Landslide Susceptibility Assessment and Model Adaptability Research. *Remote Sens.* **2024**, *16*, 2305. [CrossRef]
56. Shahabi, H.; Ahmadi, R.; Alizadeh, M.; Hashim, M.; Al-Ansari, N.; Shirzadi, A.; Wolf, I.D.; Ariffin, E.H. Landslide susceptibility mapping in a mountainous area using machine learning algorithms. *Remote Sens.* **2023**, *15*, 3112. [CrossRef]
57. Ma, S.; Shao, X.; Xu, C. Potential Controlling Factors and Landslide Susceptibility Features of the 2022 Ms 6.8 Luding Earthquake. *Remote Sens.* **2024**, *16*, 2861. [CrossRef]
58. Li, P.; Wang, H.; Li, H.; Ni, Z.; Deng, H.; Sui, H.; Xu, G. Refined Landslide Susceptibility Mapping Considering Land Use Changes and InSAR Deformation: A Case Study of Yulin City, Guangxi. *Remote Sens.* **2024**, *16*, 3016. [CrossRef]
59. Yang, J.; Huang, X. The 30 m annual land cover dataset and its dynamics in China from 1990 to 2019. *Earth Syst. Sci. Data* **2021**, *13*, 3907–3925. [CrossRef]
60. Date, O.P. *World: Internationally Agreed Glossary of Basic Terms Related to Disaster Management*; UN Department of Humanitarian Affairs: New York, NY, USA, 1992.
61. Monsieurs, E.; Jacobs, L.; Michellier, C.; Basimike Tchangaboba, J.; Ganza, G.B.; Kervyn, F.; Maki Mateso, J.-C.; Mugaruka Bibentyo, T.; Kalikone Buzera, C.; Nahimana, L.; et al. Landslide inventory for hazard assessment in a data-poor context: A regional-scale approach in a tropical African environment. *Landslides* **2018**, *15*, 2195–2209. [CrossRef]
62. Huang, F.; Mao, D.; Jiang, S.-H.; Zhou, C.; Fan, X.; Zeng, Z.; Catani, F.; Yu, C.; Chang, Z.; Huang, J.; et al. Uncertainties in landslide susceptibility prediction modeling: A review on the incompleteness of landslide inventory and its influence rules. *Geosci. Front.* **2024**, *15*, 101886. [CrossRef]
63. Chang, M.; Cui, P.; Dou, X.; Su, F. Quantitative risk assessment of landslides over the China-Pakistan economic corridor. *Int. J. Disaster Risk Reduct.* **2021**, *63*, 102441. [CrossRef]
64. Chang, M.; Dou, X.; Su, F.; Yu, B. Remote sensing and optimized neural networks for landslide risk assessment: Paving the way for mitigating Afghanistan landslide damage. *Ecol. Indic.* **2023**, *156*, 111179. [CrossRef]
65. Shah, N.A.; Shafique, M.; Ishfaq, M.; Faisal, K.; Van der Meijde, M. Integrated approach for landslide risk assessment using geoinformation tools and field data in Hindukush mountain ranges, Northern Pakistan. *Sustainability* **2023**, *15*, 3102. [CrossRef]
66. Chang, M.; Dou, X.; Tang, L.; Xu, H. Risk assessment of multi-disaster in Mining Area of Guizhou, China. *Int. J. Disaster Risk Reduct.* **2022**, *78*, 103128. [CrossRef]
67. Xiao, T.; Yin, K.; Yao, T.; Liu, S. Spatial prediction of landslide susceptibility using GIS-based statistical and machine learning models in Wanzhou County, Three Gorges Reservoir, China. *Acta Geochim.* **2019**, *38*, 654–669. [CrossRef]
68. Peng, S.; Ding, Y.; Liu, W.; Li, Z. 1 km monthly temperature and precipitation dataset for China from 1901 to 2017. *Earth Syst. Sci. Data* **2019**, *11*, 1931–1946. [CrossRef]
69. Yue, T.; Yin, S.; Xie, Y.; Yu, B.; Liu, B. Rainfall erosivity mapping over mainland China based on high-density hourly rainfall records. *Earth Syst. Sci. Data* **2022**, *14*, 665–682. [CrossRef]
70. United Nations Office for Disaster Risk Reduction (UNDRR). Report of the 2022 Global Platform for Disaster Risk Reduction. Available online: https://globalplatform.undrr.org/syndication/gp2022 (accessed on 21 October 2024).
71. Yao, Y.; Cheng, L.; Chen, S.; Chen, H.; Chen, M.; Li, N.; Li, Z.; Dongye, S.; Gu, Y.; Yi, J. Study on Road Network Vulnerability Considering the Risk of Landslide Geological Disasters in China's Tibet. *Remote Sens.* **2023**, *15*, 4221. [CrossRef]
72. Lei, Y.; Gu, H.; Cui, P. Vulnerability assessment for buildings exposed to torrential hazards at Sichuan-Tibet transportation corridor. *Eng. Geol.* **2022**, *308*, 106803. [CrossRef]
73. Luo, H.Y.; Zhang, L.M.; Zhang, L.L.; He, J.; Yin, K.S. Vulnerability of buildings to landslides: The state of the art and future needs. *Earth Sci. Rev.* **2023**, *238*, 104329. [CrossRef]
74. Li, Z.; He, W.; Cheng, M.; Hu, J.; Yang, G.; Zhang, H. SinoLC-1: The first 1 m resolution national-scale land-cover map of China created with a deep learning framework and open-access data. *Earth Syst. Sci. Data* **2023**, *15*, 4749–4780. [CrossRef]
75. Hengl, T. *Global Landform and Lithology Class at 250 m Based on the USGS Global Ecosystem Map (1.0)*; Zenodo, 2018. Available online: https://zenodo.org/records/1464846 (accessed on 21 October 2024).
76. Chen, T.; Guestrin, C. XGBoost: A Scalable Tree Boosting System. In Proceedings of the 22nd ACM SIGKDD International Conference on Knowledge Discovery and Data Mining, San Francisco, CA, USA, 13–17 August 2016; pp. 785–794.
77. Fawcett, T. An introduction to ROC analysis. *Pattern Recognit. Lett.* **2006**, *27*, 861–874. [CrossRef]
78. Zhang, T.; Huang, Y.; Liao, H.; Gong, X.; Peng, B. Short-term power forecasting and uncertainty analysis of wind farm at multiple time scales. *IEEE Access.* **2024**, *12*, 25129–25145. [CrossRef]
79. Zhang, T.; Huang, Y.; Liao, H.; Liang, Y. A hybrid electric vehicle load classification and forecasting approach based on GBDT algorithm and temporal convolutional network. *Appl. Energy* **2023**, *351*, 121768. [CrossRef]
80. Gu, B.; Zhang, T.; Meng, H.; Zhang, J. Short-term forecasting and uncertainty analysis of wind power based on long short-term memory, cloud model and non-parametric kernel density estimation. *Renew. Energy* **2021**, *164*, 687–708. [CrossRef]

81. Chen, W.; Shahabi, H.; Zhang, S.; Khosravi, K.; Shirzadi, A.; Chapi, K.; Binh Thai, P.; Zhang, T.; Zhang, L.; Chai, H.; et al. Landslide susceptibility modeling based on GIS and novel bagging-based kernel logistic regression. *Appl. Sci.* **2018**, *8*, 2540. [CrossRef]
82. Zhou, C.; Yin, K.; Cao, Y.; Ahmed, B.; Li, Y.; Catani, F.; Pourghasemi, H.R. Landslide susceptibility modeling applying machine learning methods: A case study from Longju in the Three Gorges Reservoir area, China. *Comput. Geosci.* **2018**, *112*, 23–37. [CrossRef]
83. Liang, X. Research on Meteorological Early-Warning for Landslide Risk in Wanzhou District, ThreeGorges Reservoir. Ph.D. Thesis, China Universityof Geosciences (Wuhan), Wuhan, China, 2023.
84. Xiao, L.; Wang, J.; Zhu, Y.; Zhang, J. Quantitative risk analysis of a rainfall-induced complex landslide in Wanzhou County, Three Gorges Reservoir, China. *Int. J. Disaster Risk Sci.* **2020**, *11*, 347–363. [CrossRef]
85. Wang, J.; Xiao, L.; Zhang, J.; Zhu, Y. Deformation characteristics and failure mechanisms of a rainfall-induced complex landslide in Wanzhou County, Three Gorges Reservoir, China. *Landslides* **2020**, *17*, 419–431. [CrossRef]

Disclaimer/Publisher's Note: The statements, opinions and data contained in all publications are solely those of the individual author(s) and contributor(s) and not of MDPI and/or the editor(s). MDPI and/or the editor(s) disclaim responsibility for any injury to people or property resulting from any ideas, methods, instructions or products referred to in the content.